J. Fluid Mech. (2024), *vol.* 984, A14, doi:10.1017/jfm.2024.167

JFM PAPERS

An Earth-fixed observer to ship waves

Hui Liang[1,†], **Yan Li**[2,†] **and Xiaobo Chen**[3]

[1]Technology Centre for Offshore and Marine, Singapore (TCOMS), 118411, Republic of Singapore

[2]Department of Mathematics, University of Bergen, Bergen 5007, Norway

[3]Research Department, Bureau Veritas Marine & Offshore, 4 rue Duguay Trouin, 44800 Saint Herblain, France

(Received 8 May 2023; revised 12 January 2024; accepted 19 February 2024)

This work deals with the linear surface waves generated by a vessel advancing at a constant forward speed. These waves, known as ship waves, appear stationary to an observer on the vessel. Rather than exploring the well-studied stationary ship waves, this work delves into the physical properties of ship waves measured at Earth-fixed locations. While it might have been expected that analysing these waves in an Earth-fixed coordinate system would be a straightforward transformation from existing analytical theories in a moving coordinate system, the reality proves to be quite different. The properties of waves measured at fixed locations due to a passing ship turn out to be complex and non-trivial. They exhibit unique characteristics, being notably unsteady and short crested, despite appearing stationary to an observer on the generating vessel. The analytical expressions for the physical properties of these unsteady waves are made available in this work, including the amplitude, frequency, wavenumber, direction of propagation, phase velocity and group velocity. Based on these newly derived expressions and two-point measurements, an inverse method has been presented for determining the advancing speed and the course of motion of the moving ship responsible for the wave generation. The results from this study can be used in a wide range of applications, such as interpreting data from point measurements and assessing the roles of ship waves in transporting ocean particles.

Key words: surface gravity waves, wakes

1. Introduction

The classic problem of ship waves has been extensively studied since Lord Kelvin's fascinating discovery in 1887 (Thomson 1887). Kelvin's discovery revealed a constant sector of waves, beyond which stationary ship wakes vanish in an ideal flow over deep water, as depicted in figure 1. A majority of the previous works deal with stationary waves which are seen by a moving observer together with the advancing vessel responsible for

† Email addresses for correspondence: liang_hui@tcoms.sg, yan.li@uib.no

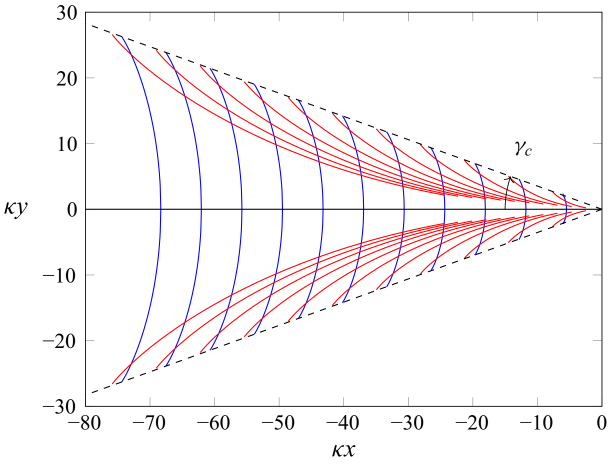

Figure 1. Wave crestlines of the Kelvin wake in the coordinate system moving with the ship composed of transverse waves (blue solid line) and divergent waves (red solid line) confined within the cusp lines (black dashed line) of Kelvin angle $\gamma_c = \arctan(1/\sqrt{8}) \approx 19^\circ 28'$; $\kappa = g/U^2$ where U denotes the ship's speed, and g is the gravitational acceleration.

the generation of these waves (see, Wehausen 1973; Reed & Milgram 2002; Li & Ellingsen 2016*b*; Yuan *et al.* 2021 among others). It has been somewhat taken for granted that investigating stationary ship waves in an Earth-fixed system only involves a transformation of the coordinate system from a moving to an Earth-fixed one. In this work, we revisit the classic problem of ship waves in the 'eyes' of an Earth-fixed observer and demonstrate that it is not as trivial as would have been imagined. Instead, we highlight that there are newly emerging needs for a deeper understanding of the underlying physics within an Earth-fixed coordinate system, as explained in detail in the following.

While the importance of ship waves has been well known in many applied engineering fields because of its relevance to the wave-making resistance of vessels, see, e.g. Yeung (1972), Beck, Newman & Tuck (1975), Nakos & Sclavounos (1990), Noblesse, Huang & Yang (2013), Li, Smeltzer & Ellingsen (2019) and He *et al.* (2021), it has been increasingly recognised in the community of coastal morphology and natural hazards in the sea and coastal waters in recent decades. In the semi-sheltered and coastal areas, waves generated by ship transits are a major source of impact on coastal environments (Forlini *et al.* 2021). They can not only erode the bank of the waterway and coastal line, but also pose a potential hazardous impact on coastal structures or berthed floating bodies (Bourne 2000; Soomere 2007; Rapaglia *et al.* 2015; Gabel, Lorenz & Stoll 2017; Scarpa *et al.* 2019). An advancing vessel can act as a source of propagating wake wash, generating wakes that force sediment transport and drive vertical mixing, which is important to aquatic ecosystems (Rapaglia *et al.* 2015; Gabel *et al.* 2017; Meyers *et al.* 2021). Thereby, how to quantify the impact of ship wakes on the coastal environments is an open and essential question for coastal management and protection. The answer to this question greatly relies on an in-depth physical understanding of ship wakes measured at fixed locations, which has not been fully available due to limited studies. To this end, this work aims to fill in the knowledge gaps.

There are available methods that have been developed for retrieving the physical properties of ship waves measured at fixed locations. One such, the method of short-time Fourier transform with respect to a record of time series, was pioneered by

Wyatt & Hall (1988) and has been widely used in processing wave probe measurements in the last decade (Didenkulova *et al.* 2013; Sheremet, Gravois & Tian 2013; Torsvik *et al.* 2015; Pethiyagoda, McCue & Moroney 2017). Sheremet *et al.* (2013) utilised the short-time Fourier transform to investigate the statistics regarding measured ship wakes, identifying an up-chirping frequency component. Moreover, it has been used in the cases of water of finite depth (Pethiyagoda *et al.* 2018) and more general cases where the ship advances at a non-constant speed (Pethiyagoda *et al.* 2021).

Compared with other remote sensing techniques, such as satellite photography (Liu, Peng & Chang 1997; Rabaud & Moisy 2013) and synthetic aperture radar (Lyden *et al.* 1988; Reed & Milgram 2002; Karakuş, Rizaev & Achim 2020), a distinctive feature of the method is the simplicity at an adequate level of accuracy since it only requires one-point measurement. It can especially lead to the amplitude of waves with different frequencies. This approach relying on one-point measurements particularly facilitates the analysis of wave amplitudes across different frequencies by steadily advancing sailing ships. Torsvik *et al.* (2015) reported that the measured linear waves contain two different components: one with a constant frequency and the other with increasing frequency corresponding to transverse and divergent waves, respectively. They established a correlation between wave frequency, propagation direction, ship speed and distance from the sailing line. The second-order nonlinear ship waves can lead to four extra frequencies, according to Pethiyagoda *et al.* (2017). The time-frequency heat maps are obtained by Buttle *et al.* (2022) for waves generated by slender ships, which are validated through comparisons with the experimental findings reported by Buttle *et al.* (2020). The same experimental results from waves measured by an array of fixed probes are also used to validate the theory derived from this work.

When a ship passes different physical locations, ring waves are generated at each of the ship locations (Li & Ellingsen 2015, 2016*a*). These waves can pass a fixed location with different frequencies as their origins are different due to the time-varying positions of the ship relative to the fixed location which measures the (unsteady) ship waves (see, e.g. Liang, Santo & Si 2022; Liang, Li & Chen 2023). This physical process means the need for more than just measuring the amplitude and frequency of ship waves at a particular location. There are more essential physical properties that are desired, especially the fluid particle velocities and the direction of wave propagation due to passing ship waves. To this end, novel approaches are required to complement the available aforementioned methods. This study will focus on introducing a novel approximate method to address these requirements.

In summary, the objective of this work is threefold. Firstly, we aim to provide a clear explanation of the conditions under which ship waves can pass a fixed location. Secondly, based on these conditions, we derive explicit expressions for various physical properties of these waves, such as amplitude, wave incidence angle, group and phase velocity and fluid particle velocities resulting from passing ship waves. In contrast to the limitations of time–frequency spectrograms, which can only estimate wave amplitude, our analytical expressions enable straightforward estimations of multiple physical quantities. Notably, we demonstrate that the amplitudes of transverse and divergent waves measured at a fixed location can also be expressed using the Kochin function, which is associated with the geometry of the ship hull. Thirdly, leveraging the analytical expressions for physical quantities, we propose a novel method that relies on measurements from two probes fixed at distinct locations to determine the speed and direction of the vessel responsible for generating the observed waves. This approach offers an efficient and accurate means of vessel tracking, allowing for practical applications in maritime management.

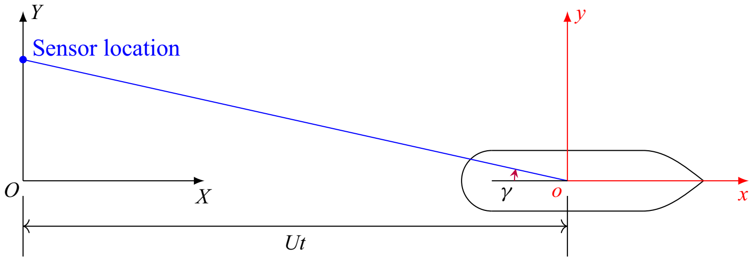

Figure 2. Definition of global and local coordinate systems. The global coordinate system $OXYZ$ is fixed in space, and the sensor is located at $(X, Y) = (0, Y_s)$. The local coordinate system moves steadily with the ship at a constant speed U. At $t = 0$, the two coordinate systems coincide.

The layout of the present paper is as follows. In § 2, waves generated by a ship hull are modelled by a Hogner model (Hogner 1923) in conjunction with the viscous-ship-wave Green function (Liang & Chen 2019). As a sequel to § 2, a uniform Kelvin–Havelock–Peters (KHP) asymptotic approximation (Wu *et al.* 2018; Liang *et al.* 2020*b*) is employed in § 3 to explicitly decompose the wave pattern inside the Kelvin wake into transverse and divergent waves. In § 4, physical quantities for both transverse and divergent waves propagating in an Earth-fixed frame of reference are derived, and the long-time asymptotic behaviours are discussed. Building upon the physical properties of transverse and divergent waves, a two-probe method is developed to determine the ship's speed and sailing direction in § 5. The results, particularly the underlying physics, are discussed in § 6. Concluding remarks and future perspectives are presented in § 7.

2. Description of ship waves

In this section, we focus on the description of linear surface waves generated by a steadily advancing object. We employ the viscous-ship-wave Green function, which satisfies the linear free surface boundary condition, to construct the solution as discussed in § 2.2. Additionally, we adopt the Hogner model, as presented in § 2.3, to simulate the free surface flows around the ship hull.

2.1. *Statement of the problem*

Stationary waves from the perspective of an observer positioned on the ship responsible for the generation of the waves are described. To distinguish these waves from those measured at fixed locations, we consider two frames of reference, as illustrated in figure 2.

The first frame of reference corresponds to an Earth-fixed Cartesian coordinate system $OXYZ$, where the OX axis points in the direction of the ship's bow and the OZ axis points upward. In this system, the ship moves at a constant speed U along the positive OX direction. The second coordinate system $oxyz$ moves with the ship, and its origin is fixed at the centre of the ship. Consequently, we establish the relationships $x = X - Ut$, $Y = y$ and $Z = z$, which relate the coordinates in the two frames of reference.

In the moving coordinate system $oxyz$, the physical problem is steady, and can be defined as a ship hull in the presence of a uniform stream with a velocity U in the direction of the negative ox axis. Then, the velocity potential Φ in the flow field is

$$\Phi(x, y, z) = U[-x + \phi(x, y, z)], \tag{2.1}$$

where ϕ denotes the potential disturbed by the presence of ship hull.

The perturbed potential ϕ satisfies the linearised Kelvin–Michell free surface condition with viscous effects (Dias, Dyachenko & Zakharov 2008; Liang & Chen 2019)

$$U^2\frac{\partial^2\phi}{\partial x^2}+g\frac{\partial\phi}{\partial z}+4\nu_0U\frac{\partial^3\phi}{\partial x\partial z^2}=0,\quad \text{at } z=0, \tag{2.2}$$

where ν_0 denotes the kinematic fluid viscosity coefficient. The combined boundary condition on a still water surface given by (2.2) is based on the weakly damped free surface flow theory, see, e.g. Dias *et al.* (2008) for details. The magnitude of the viscous term in this condition is negligibly small compared with the remaining terms (Liang & Chen 2019). This suggests the flow considered is nearly irrotational, thereby the velocity potential in the statement of the (far-field) ship-wave problem is interpreted as a leading-order approximation. The body boundary condition on the hull surface is given by

$$\frac{\partial\phi}{\partial n}=n_x, \tag{2.3}$$

where the normal vector is defined as positive pointing inwards to the fluid domain. The unknown velocity potential in the viscous boundary condition on a still water surface and the wet surface of the ship hull in calm water given by (2.2) and (2.3), respectively, is solved through a viscous-ship-wave Green function presented in § 2.2 combined with a Hogner model detailed in § 2.3.

2.2. *Viscous-ship-wave Green function*

The viscous-ship-wave Green function derived by Liang & Chen (2019) is reviewed in this section, which, taking into account the fluid viscosity, represents the flow induced by a point singularity with unit strength, translating steadily along a straight path in calm water. We remark that such a Green function especially has the feature of removing non-physical behaviours of the classic ship-wave Green function, see, e.g. Ursell (1960), Clarisse & Newman (1994) and Chen & Wu (2001). For example, unbounded wave amplitudes in the region near the course of the moving point singularity.

Following Liang & Chen (2019), the viscous-ship-wave Green function satisfying the free surface condition (2.2) is written as

$$4\pi G(\boldsymbol{x},\boldsymbol{\xi})=-1/r+1/d+G^F,\quad \text{with } \begin{Bmatrix} r\\ d\end{Bmatrix}=\sqrt{(x-\xi)^2+(y-\eta)^2+(z\mp\zeta)^2}, \tag{2.4}$$

where $\boldsymbol{x}\equiv(x,y,z)$ and $\boldsymbol{\xi}\equiv(\xi,\eta,\zeta)$ denote the flow-field point and source point, respectively, and G^F is the free surface term in the form of a double Fourier integral. The free surface term $G^F=G^L+G^W$ can be decomposed into a non-oscillatory local-flow component G^L and a wave component G^W dominant in the far field (see Appendix A for details). The local-flow component G^L is

$$G^L=\frac{2\kappa}{\pi}\mathrm{Im}\int_{-1}^{1}\mathrm{e}^{Z}E_1(Z)\,\mathrm{d}q, \tag{2.5a}$$

with

$$Z=-\mathrm{i}\kappa\sqrt{1-q^2}\left[-|x-\xi|+\mathrm{i}\sqrt{1-q^2}(z+\zeta)-\mathrm{i}q(y-\eta)\right], \tag{2.5b}$$

and the wave component G^W is

$$G^W = -4H(\xi - x)\mathrm{Im}\int_{-\infty}^{\infty} \kappa\mathcal{E}(\boldsymbol{x}, q)\tilde{\mathcal{E}}(\boldsymbol{\xi}, q)\,\mathrm{d}q, \tag{2.6a}$$

with

$$\mathcal{E}(\boldsymbol{x}, q) = \exp\left[\kappa(1+q^2)z + 4\epsilon\kappa x\frac{(1+q^2)^3}{1+2q^2} - \mathrm{i}\kappa\sqrt{1+q^2}(x+qy)\right], \tag{2.6b}$$

$$\tilde{\mathcal{E}}(\boldsymbol{\xi}, q) = \exp\left[\kappa(1+q^2)\zeta - 4\epsilon\kappa\xi\frac{(1+q^2)^3}{1+2q^2} + \mathrm{i}\kappa\sqrt{1+q^2}(\xi+q\eta)\right], \tag{2.6c}$$

where $\mathrm{e}^u E_1(u)$ is the complex exponential-integral function (Abramowitz & Stegun 1964), ϵ is a parameter associated with viscous effects defined as $\epsilon = g\nu_0/U^3$ and κ is defined as $\kappa = g/U^2$, which can be interpreted as the wavenumber along the ship's track. In (2.6*a*), $H(u)$ means the Heaviside step function, which equals to 1 for $u > 0$, or 0 otherwise.

2.3. *Hogner model*

The Hogner model due to Hogner (1923) has been widely used to express the unknown velocity potential, ϕ, in an explicit form. It has been tested and proven to be adequate in approximating linear ship waves (Zhang *et al.* 2015; Wu *et al.* 2019; Buttle *et al.* 2022).

Following Hogner (1923), the velocity potential due to the flow induced by an advancing ship hull is represented by a source distribution with strength n_ξ over the mean wetted hull surface denoted by $\varSigma^H(\xi, \eta, \zeta)$

$$\phi(\boldsymbol{x}) = \iint_{\varSigma^H} n_\xi G(\boldsymbol{x}, \boldsymbol{\xi})\,\mathrm{d}S, \tag{2.7}$$

where n_ξ is the component in the x-direction of the vector normal to the ship's hull. Introducing polar coordinates $(x, y) \equiv R(-\cos\gamma, \sin\gamma)$, where γ is measured from the negative x-axis in the clockwise direction (figure 2), the free surface elevation, denoted by $E(x, y)$, at a location far away from the ship where $R/L \gg 1$, is written in the Fourier–Kochin form given by

$$\begin{aligned} E(x, y) &= \frac{1}{\kappa}\left.\frac{\partial\phi}{\partial x}\right|_{z=0} \approx \frac{1}{4\pi\kappa}\iint_{\varSigma^H} n_\xi \left.\frac{\partial G^W(\boldsymbol{x}, \boldsymbol{\xi})}{\partial x}\right|_{z=0}\mathrm{d}S \\ &= \frac{\kappa}{\pi}\mathrm{Re}\int_{-\infty}^{\infty} K(q, x)\exp[\mathrm{i}\kappa R\psi(q, \gamma)]\,\mathrm{d}q, \end{aligned} \tag{2.8}$$

where G^W is the wave component given by (2.6*a*). In the wavenumber (q) integral (2.8), $K(q, x)$ is the Kochin function determined by the ship hull geometry written as

$$K(q, x) = \sqrt{1+q^2}\exp\left[4\epsilon\kappa x\frac{(1+q^2)^3}{1+2q^2}\right]\iint_{\varSigma^H} n_\xi H(\xi - x)\tilde{\mathcal{E}}(\boldsymbol{\xi}, q)\,\mathrm{d}S, \tag{2.9}$$

and the phase function $\psi(q, \gamma)$ by

$$\psi(q, \gamma) = \sqrt{1+q^2}(\cos\gamma - q\sin\gamma), \tag{2.10}$$

consistent with that in (2.6*b*). The velocity vector due to the ship-motion-induced flow, denoted by $\boldsymbol{u} = [u^x, u^y, u^z]^{\mathrm{T}}$, can be obtained from the velocity potential through

$$\begin{aligned} \boldsymbol{u} \equiv \nabla \phi(\boldsymbol{x}) &= \iint_{\Sigma^H} n_\xi \nabla_{\boldsymbol{x}} G(\boldsymbol{x}, \boldsymbol{\xi})\, \mathrm{d}S \\ &\approx \frac{\kappa^2}{\pi} \mathrm{Re} \int_{-\infty}^{\infty} \begin{bmatrix} 1 \\ q \\ \mathrm{i}\sqrt{1+q^2} \end{bmatrix} K(q, x) \exp(\kappa[(1+q^2)z + \mathrm{i}R\psi(q, \gamma)])\, \mathrm{d}q. \end{aligned} \tag{2.11}$$

3. Decomposition of transverse and divergent waves

As is widely known, the stationary ship wake consists of both transverse and divergent waves which have different physical features (Li 2018; Liang & Chen 2018). Based on the surface elevation given by (2.8), we derive a new approximation to (2.8) in the far field, permitting the explicit partition of ship waves into the transverse and divergent waves. This is achieved through the use of the KHP approximation, whose advantageous features compared with other approximations can be found in other works e.g. Liang *et al.* (2020*b*) and Wu *et al.* (2018). The application of the asymptotic approximation indicates that the waves in the far field are concerned. This implies that we neglect the effects of ship bow waves, which typically exhibit strong nonlinear behaviour. Nevertheless, the bow waves are confined to the vicinity of the ship, and thus it is sensible to neglect their effects in the far field (Fontaine, Faltinsen & Cointe 2000).

3.1. *Stationary phase points and saddle points*

Within the Kelvin wake, characterised by polar angles $\gamma < \gamma_c \equiv 19^\circ 28'$, there are two distinct stationary phase points requiring the vanishing of the first-order derivative of the phase function, i.e. $\psi'(q, \gamma) = 0$, where the prime $'$ means differentiation with variable q. Then, the stationary phase points are given by

$$q_\pm = (1 \pm Q) \cot \gamma / 4, \quad \text{with } Q = \sqrt{1 - 8\tan^2 \gamma}, \tag{3.1}$$

and the corresponding second-order derivatives are

$$\psi''_\pm \equiv \frac{\partial^2 \psi(q_\pm, \gamma)}{\partial q^2} = \mp \frac{4}{\sqrt{3}} \frac{Q \sin \gamma}{\sqrt{(1 \pm Q)(1 \mp Q/3)}}, \tag{3.2}$$

where subscripts '$-$' and '$+$' correspond to transverse and divergent waves, respectively, hereafter.

At the cusp line of the Kelvin wake $\gamma = \gamma_c = \arctan(1/\sqrt{8})$, two stationary phase points coalesce $q_- = q_+ = q_c = 1/\sqrt{2}$, and both first- and second-order derivatives of the phase function are nil, e.g. $\psi'(q_c, \gamma_c) = \psi''(q_c, \gamma_c) = 0$. The third- and fourth-order derivatives at q_c are

$$\psi'''_c \equiv \frac{\partial^3 \psi(q_c, \gamma_c)}{\partial q^3} = -4\sqrt{6}/9, \quad \text{and} \quad \psi''''_c \equiv \frac{\partial^4 \psi(q_c, \gamma_c)}{\partial q^4} = 8\sqrt{3}/9. \tag{3.3a,b}$$

Outside the Kelvin wake, when $\gamma > \gamma_c$, the two stationary phase points transform into two complex saddle points, forming a complex conjugate pair. To evaluate the integral, the integration path is deformed, and only the contribution from the saddle point with an imaginary part of ψ'' that is positive matters. The selected saddle point is

$$q_o = (1 - \mathcal{Q}) \cot \gamma / 4, \quad \text{with } \mathcal{Q} = \mathrm{i}\sqrt{8 \tan^2 \gamma - 1}, \tag{3.4}$$

and the corresponding second-order derivative is

$$\psi''_o \equiv \frac{\partial^2 \psi(q_o, \gamma)}{\partial q^2} = \frac{4}{\sqrt{3}} \frac{\mathcal{Q} \sin \gamma}{\sqrt{(1 - \mathcal{Q})(1 + \mathcal{Q}/3)}}. \tag{3.5}$$

3.2. *Decomposition via the KHP approximation*

The KHP approximation has been extensively studied in Wu *et al.* (2018) and Liang *et al.* (2020*b*), delving into mathematical derivations and accuracy assessments. However, these works predominantly focus on the mathematical aspects rather than investigating the physical perspective. One notable advantage of the KHP approximation over other counterparts, Chester–Friedman–Ursell (CFU) approximation (Chester, Friedman & Ursell 1957), is its ability to decompose the wave pattern within the Kelvin wedge into transverse and divergent waves, a facet not considered in Wu *et al.* (2018) and Liang *et al.* (2020*b*). This subsection aims to concentrate specifically on this aspect, elucidating the wave pattern decomposition via the KHP approximation.

Based on Liang *et al.* (2020*b*), the KHP approximations to the surface elevation, E, and velocity vector $\boldsymbol{u} = [u^x, u^y, u^z]^{\mathrm{T}}$ in the flow region inside the cusp of the Kelvin wake $\gamma \leq \gamma_c$ are expressed as

$$\begin{bmatrix} E(x,y) \\ u^x(\boldsymbol{x}) \\ u^y(\boldsymbol{x}) \\ u^z(\boldsymbol{x}) \end{bmatrix} = \begin{bmatrix} E_+(x,y) \\ u^x_+(\boldsymbol{x}) \\ u^y_+(\boldsymbol{x}) \\ u^z_+(\boldsymbol{x}) \end{bmatrix} + \begin{bmatrix} E_-(x,y) \\ u^x_-(\boldsymbol{x}) \\ u^y_-(\boldsymbol{x}) \\ u^z_-(\boldsymbol{x}) \end{bmatrix}$$

$$\text{with} \begin{bmatrix} E_\pm(x,y) \\ u^x_\pm(\boldsymbol{x}) \\ u^y_\pm(\boldsymbol{x}) \\ u^z_\pm(\boldsymbol{x}) \end{bmatrix} = \mathrm{Re}\left\{ \begin{bmatrix} \mathcal{E}_\pm \\ \mathcal{U}^x_\pm \\ \mathcal{U}^y_\pm \\ \mathcal{U}^z_\pm \end{bmatrix} \exp[\mathrm{i}(\kappa R \psi_\pm \mp \pi/4)] \right\}, \tag{3.6}$$

where $\boldsymbol{x} \equiv (x, y, z)$ with the horizontal coordinates further expressed by $(x, y) \equiv R(-\cos\gamma, \sin\gamma)$, and the components $[\mathcal{E}_\pm, \mathcal{U}^x_\pm, \mathcal{U}^y_\pm, \mathcal{U}^z_\pm]^{\mathrm{T}}$ are

$$\begin{bmatrix} \mathcal{E}_\pm \\ \mathcal{U}^x_\pm \\ \mathcal{U}^y_\pm \\ \mathcal{U}^z_\pm \end{bmatrix} = \frac{\kappa}{\pi} \left[\frac{\sqrt{2\pi}}{\sqrt{\kappa R |\psi''_\pm|}} (1 - \mathrm{e}^{-a^{4/3}}) \boldsymbol{K}(q_\pm, \boldsymbol{x}) + \frac{C^*_H \mathrm{e}^{-a^{4/3}}}{(\kappa R |\psi'''_c|)^{1/3}} (1 \mp \mathscr{F}) \boldsymbol{K}(q_c, \boldsymbol{x}) \right], \tag{3.7}$$

with $C_H^* \equiv \Gamma(1/3)/6^{1/6} \approx 1.987334$ and $a = 3\kappa R|\psi(q_+) - \psi(q_-)|/4$. In (3.7), the vector function $\boldsymbol{K}$ is defined as

$$\boldsymbol{K}(q, \boldsymbol{x}) \equiv \begin{bmatrix} \mathcal{K}^e(q, \boldsymbol{x}) \\ \mathcal{K}^x(q, \boldsymbol{x}) \\ \mathcal{K}^y(q, \boldsymbol{x}) \\ \mathcal{K}^z(q, \boldsymbol{x}) \end{bmatrix} = \begin{bmatrix} K(q, x) \\ \kappa K(q, x)\, \mathrm{e}^{\kappa(1+q^2)z} \\ \kappa q\, K(q, x)\, \mathrm{e}^{\kappa(1+q^2)z} \\ \mathrm{i}\,\kappa\,\sqrt{1+q^2}\, K(q, x)\, \mathrm{e}^{\kappa(1+q^2)z} \end{bmatrix}, \tag{3.8}$$

and $\mathscr{F}$ is an operator to a function χ with $\chi = \mathcal{K}^e, \mathcal{K}^x, \mathcal{K}^y$ or $\mathcal{K}^z$, defined as

$$\mathscr{F}(\chi) = \frac{\Gamma(2/3)}{\Gamma(1/3)} \left(\left.\frac{\partial \chi}{\partial q}\right|_{q=q_c} - \frac{\psi_c''''}{6\psi_c'''}\chi \right) \left(\frac{6}{\kappa R \psi_c'''} \right)^{1/3}, \tag{3.9}$$

where $\Gamma(u)$ denotes the gamma function (Abramowitz & Stegun 1964).

Equation (3.6) provides an explicit decomposition of the two systems of waves consisting of transverse waves E_- and divergent waves E_+ as well as their induced velocity vector $\boldsymbol{u}_-$ and $\boldsymbol{u}_+$, respectively. At the cusp line of the Kelvin wake, there is a phase difference $\pi/2$ of transverse and divergent waves.

The approximation to wave pattern and velocity components outside the cusp of the Kelvin wake $\gamma \geq \gamma_c$ is written as

$$\begin{bmatrix} E(x, y) \\ u^x(\boldsymbol{x}) \\ u^y(\boldsymbol{x}) \\ u^z(\boldsymbol{x}) \end{bmatrix} = \mathrm{Re}\left\{ \begin{bmatrix} \mathcal{E}_o \\ \mathcal{U}_o^x \\ \mathcal{U}_o^y \\ \mathcal{U}_o^z \end{bmatrix} \exp[\mathrm{i}(\kappa R \psi_o + \pi/4)] \right\}, \tag{3.10}$$

where the components $[\mathcal{E}_o, \mathcal{U}_o^x, \mathcal{U}_o^y, \mathcal{U}_o^z]^{\mathrm{T}}$ are

$$\begin{bmatrix} \mathcal{E}_o \\ \mathcal{U}_o^x \\ \mathcal{U}_o^y \\ \mathcal{U}_o^z \end{bmatrix} = \frac{\kappa}{\pi} \left[\frac{\sqrt{2\pi}}{\sqrt{\kappa R |\psi_o''|}} (1 - \mathrm{e}^{-b^{4/3}}) \boldsymbol{K}(q_o, \boldsymbol{x}) + \frac{(1-\mathrm{i}) C_H^* \mathrm{e}^{-b^{4/3}}}{(\kappa R |\psi_c'''|)^{1/3}} (\mathrm{e}^{-2b/3} + \mathrm{i}\mathscr{F}) \boldsymbol{K}(q_c, \boldsymbol{x}) \right], \tag{3.11}$$

with $b = 3\kappa R|\mathrm{Im}(\psi_o'')|/2$.

4. Physical properties of ship waves

In the frame of reference moving with the ship, the physics of ship waves is well understood (Lighthill 1978). The wave pattern, comprising transverse and divergent waves behind the ship, is stationary, meaning it does not change with time. The phase velocity of stationary waves is observed as zero. In contrast, from the perspective of a fixed observer, ship waves are unsteady and the phase velocity in the direction at right angles to wave crests is to be evaluated. It is typical for the propagation direction of stationary ship waves to differ from the direction of the ship motion (Noblesse *et al.* 2014; Li 2018). Physically, this implies these stationary waves have different angular frequencies. Therefore, in the Earth-fixed coordinate system, the ship waves are time dependent and particularly short crested, as elaborated in this section. In this section, our focus is placed on deriving the physical properties of propagating transverse and divergent waves, such as wave amplitude, frequency, wave heading, phase velocity and group velocity, based on the asymptotic approximations derived in § 3.

4.1. *Physical properties of transverse and divergent waves*

In the Earth-fixed coordinate system $OXYZ$, as in figure 2, the free surface elevation induced by a passing ship is

$$E(X, Y, t) = E_+(X, Y, t) + E_-(X, Y, t), \tag{4.1}$$

with E_- and E_+ denoting transverse and divergent waves given by (3.6) written in the form of

$$E_\pm(X, Y, t) = \|\mathcal{E}_\pm\| \cos[P_\pm(X, Y, t)], \tag{4.2}$$

where the phase functions $P_\pm(X, Y, t)$ are

$$P_\pm(X, Y, t) = \kappa\sqrt{1+q_\pm^2}(Ut - X - q_\pm Y) \mp \pi/4 + \mathrm{Arg}(\mathcal{E}^\pm), \tag{4.3}$$

where $\mathrm{Arg}(\mathcal{E}^\pm)$ means the argument of the complex function $\mathcal{E}^\pm$ given by (3.7).

Suppose that the sensor location is at $(X, |Y|) = (0, Y_s)$ in the fixed coordinate system, and the coordinates in the moving frame of reference are $(x, |y|) = (-Ut, Y_s)$. Here, Y_s is larger than 0, which means the sensor will not be located on the track. Following Pethiyagoda *et al.* (2017), we can define a non-dimensional time

$$\tau \equiv Ut/Y_s = -x/|y|. \tag{4.4}$$

According to the geometrical relation $\tan\gamma_c = 1/\sqrt{8}$, as in figure 1, the observation point is located inside the Kelvin wake when $\tau > \sqrt{8}$, and the cusp line of the Kelvin wake meets the sensor at $\tau = \sqrt{8}$.

Based on the phase function (4.3), we obtain the frequencies of transverse waves ω_- and divergent waves ω_+ measured at the sensor location $(X, Y) = (0, Y_s)$

$$\omega_\pm = \kappa U\sqrt{1+q_\pm^2} = \frac{\sqrt{2}g}{4U}\sqrt{\tau^2 + 4 \pm \tau\sqrt{\tau^2 - 8}}, \tag{4.5}$$

which are consistent with the results by Pethiyagoda *et al.* (2017) obtained from the geometrical relation of the dispersion relation.

Given the non-dimensional time τ defined in (4.4), the stationary phase points $q_\pm$ given by (3.1) become

$$q_\pm = \frac{\tau \pm \sqrt{\tau^2 - 8}}{4}. \tag{4.6}$$

According to the phase function given by (4.3), the wavenumbers in the X- and Y-directions are obtained

$$k_\pm^X = \kappa\sqrt{1+q_\pm^2} = \kappa\sqrt{\frac{\tau^2 + 4 \pm \tau\sqrt{\tau^2 - 8}}{8}}, \tag{4.7a}$$

and

$$k_\pm^Y = \kappa q_\pm\sqrt{1+q_\pm^2} = \kappa\frac{\tau \pm \sqrt{\tau^2 - 8}}{4}\sqrt{\frac{\tau^2 + 4 \pm \tau\sqrt{\tau^2 - 8}}{8}}, \tag{4.7b}$$

where superscripts 'X' and 'Y' indicate the X- and Y-directions, respectively, hereafter. Furthermore, we can rewrite the frequencies (4.5) as

$$\omega_{\pm} = \sqrt{g\sqrt{(k^X_{\pm})^2 + (k^Y_{\pm})^2}} = \sqrt{gk_{\pm}}, \tag{4.8}$$

by using (4.7), and with

$$k_{\pm} = \sqrt{(k^X_{\pm})^2 + (k^Y_{\pm})^2}, \tag{4.9}$$

called the wavenumber modulus. Equation (4.8) indicates that both transverse and divergent waves satisfy the deep water dispersion relation $\omega^2 = gk$ (Newman 1977).

According to (4.7), the heading angles of transverse and divergent waves can be determined

$$\beta_{\pm} = \arctan\left(\frac{k^Y_{\pm}}{k^X_{\pm}}\right) = \arctan\left(\frac{\tau \pm \sqrt{\tau^2 - 8}}{4}\right). \tag{4.10}$$

Equation (4.10) is consistent with the results by Torsvik *et al.* (2015), which are obtained from the analysis of the dispersion relation.

Given the dispersion relation (4.8), i.e. the relationship between frequency and wavenumbers, the phase velocity vector is obtained

$$\begin{aligned} \boldsymbol{c}_{\pm} = (c^X_{\pm}, c^Y_{\pm}) = \frac{\omega_{\pm}}{k_{\pm}} \frac{(k^X_{\pm}, k^Y_{\pm})}{k_{\pm}} &= \frac{U}{1 + q^2_{\pm}}(1, q_{\pm}) \\ &= \frac{8U}{\tau^2 + 4 \pm \tau\sqrt{\tau^2 - 8}}\left(1, \frac{\tau \pm \sqrt{\tau^2 - 8}}{4}\right), \end{aligned} \tag{4.11}$$

and the group velocity vector according to Lighthill (1978) is written as

$$\boldsymbol{v}_{\pm} = \left(\frac{\partial \omega_{\pm}}{\partial k^X_{\pm}}, \frac{\partial \omega_{\pm}}{\partial k^Y_{\pm}}\right) = \frac{U}{2(1 + q^2_{\pm})}(1, q_{\pm}) \equiv \frac{\boldsymbol{c}_{\pm}}{2}, \tag{4.12}$$

by differentiating the dispersion relation (4.8).

Consistent with the deep water wave theory, (4.11) and (4.12) indicate that, in the fixed coordinate system, the phase velocity of both transverse and divergent waves aligns with the direction of the group velocity and is twice the magnitude of the group velocity. These results are consistent with the theory of gravity waves in deep water, further reinforcing the validity of the derived expressions for phase and group velocities in the present study.

It is worth mentioning that (4.5) is consistent with the results determined by the geometrical analysis of the dispersion relation in Pethiyagoda *et al.* (2017). This work has in addition offered an analytical expression for the two components of the wave vectors of the ship waves passing a fixed position, i.e. (4.7*a*,*b*). Doing so permits wave directions to be readily resolved, and thereby builds a foundation for the inverse method presented in § 5. Moreover, Torsvik *et al.* (2015) have also derived a geometric relation of the wave dispersion relation, the advancing direction of ship motion and the distance of a fixed location to a ship's sailing line in the Earth-fixed coordinate. How the various frequencies measured at the fixed position are related to the transverse and diverging ship waves was not revealed in Torsvik *et al.* (2015) but has been derived analytically by this work, see, e.g. (4.8).

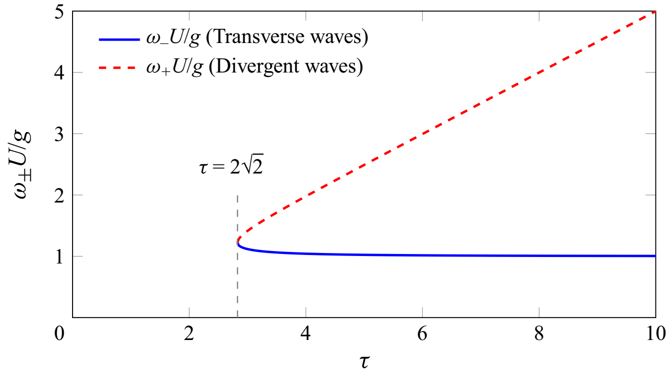

Figure 3. Normalised frequencies due to transverse waves $\omega_{-}U/g$ and divergent waves $\omega_{+}U/g$ determined by (4.5) vs non-dimensional time $\tau = Ut/Y_s$.

4.2. *Long-time asymptotic expressions*

The long-time asymptotic approximations for physical quantities derived in § 4.1 are considered here. The long-time asymptotic expressions for frequencies given by (4.5) are

$$\omega_{-} = g/U + O(\tau^{-2}), \quad \text{and} \quad \omega_{+} = g\tau/(2U) + O(\tau^{-3}) = gt/(2Y_s) + O(\tau^{-3}). \tag{4.13a,b}$$

Figure 3 displays the normalised frequencies due to transverse waves $\omega_{-}U/g$ and divergent waves $\omega_{+}U/g$ at a sensor location as a function of non-dimensional time $\tau = Ut/Y_s$, as determined by (4.5).

At $\tau = 2\sqrt{2}$, the time instant when the cusp line of the Kelvin wake intersects the sensor, the frequencies of transverse and divergent waves are identical, with a normalised frequency of $\omega_{-}U/g = \omega_{+}U/g = \sqrt{3/2}$.

With the time marching, the scaled frequency $\omega_{-}U/g$ of transverse waves remains nearly constant, as indicated by (4.13*a*,*b*). On the other hand, the scaled frequency of divergent waves $\omega_{+}U/g$ keeps increasing, in a manner linearly proportional to τ.

When τ is large, as in (4.13*a*,*b*), we have $\omega_{-} = g/U$, which indicates that the frequency of transverse waves is independent of time t, and inversely proportional to the ship's speed U. For divergent waves, however, the frequency is $\omega_{+} = gt/(2Y_s)$, linearly proportional to the time t but independent of the ship's speed U. These long-time properties offer valuable insights into the dynamics of transverse and divergent waves over time and enable us to better analyse the time–frequency spectrogram, which will be elucidated in § 5.

In the same manner, the long-time asymptotic expressions for wave incidence angles are

$$\tan(\beta_{-}) = 0 + O(\tau^{-1}) \quad \text{and} \quad \tan(\beta_{+}) = \tau/2 + O(\tau^{-1}). \tag{4.14a,b}$$

Figure 4 shows the heading angles of transverse and divergent waves at a fixed location varying with the non-dimensional time. When the sensor meets the cusp line of the Kelvin wake at $\tau = 2\sqrt{2}$, denoted by the vertical dashed line, the wave heading angles for transverse and divergent waves are identical, and equal to $\arctan(\sqrt{2}/2) \approx 35.26^{\circ}$, which agrees with the study by Torsvik *et al.* (2015). With the time marching, the incidence angle of transverse waves decreases, while that of divergent waves increases. At large non-dimensional times, the long-time asymptotic expressions in (4.14*a*,*b*) apply. Accordingly, the transverse waves eventually propagate along the sailing direction, while the divergent waves propagate perpendicular to the sailing line.

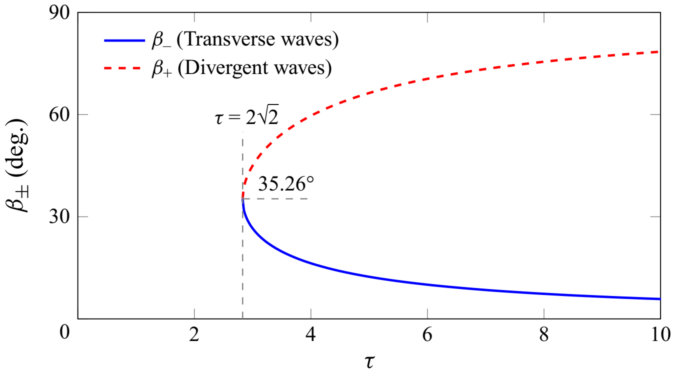

Figure 4. Heading angles of transverse waves β_- and divergent waves β_+ determined by (4.10) as a function of the non-dimensional time $\tau = Ut/Y_s$.

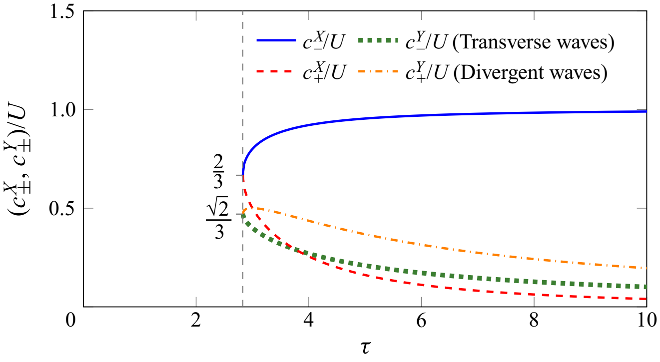

Figure 5. Phase velocity of transverse waves $\boldsymbol{c}_-$ and divergent waves $\boldsymbol{c}_+$ determined by (4.11) vs the non-dimensional time $\tau = Ut/Y_s$.

Then, the long-time asymptotic expressions for phase velocities given by (4.3) are

$$\boldsymbol{c}_- = U(1, 1/\tau) + O(\tau^{-2}) \quad \text{and} \quad \boldsymbol{c}_+ = U(4/\tau^2, 2/\tau) + O(\tau^{-3}), \tag{4.15a,b}$$

and those for group velocities given by (4.12) are

$$\boldsymbol{v}_- = U[1/2, 1/(2\tau)] + O(\tau^{-2}) \quad \text{and} \quad \boldsymbol{v}_+ = U(2/\tau^2, 1/\tau) + O(\tau^{-3}). \tag{4.16a,b}$$

Due to the fact that the group velocity is in alignment with the phase velocity, and is half the phase velocity in magnitude, only the phase velocity is discussed here. Figure 5 depicts the phase velocity of transverse and divergent waves, determined by (4.11), with respect to the non-dimensional time $\tau = Ut/Y_s$. Notably, when the cusp line intersects the sensor $\tau = 2\sqrt{2}$, the in-line and lateral phase velocity components become identical for both transverse and divergent waves. Specifically, the normalised in-line component of the phase velocity is $2/3$, while the lateral component is $\sqrt{2}/3$.

As the time progresses, as shown in (4.15a,b), the in-line phase velocity of transverse waves (c^X_-) at the sensor location eventually becomes identical to the ship's translating speed. Meanwhile, the lateral phase velocity (c^Y_-) decreases in proportion to the inverse of the non-dimensional time ($\tau = Ut/Y_s$) for transverse waves. However, for divergent waves, both the longitudinal and lateral phase velocities at the sensor location decrease over time. Specifically, the longitudinal phase velocity of divergent waves (c^X_+) decreases with the inverse square of the non-dimensional time, leading to a rapid decay rate, as illustrated in figure 5. This decrease indicates a significant change in the behaviour of divergent waves as time advances.

4.3. *Velocity components of the fluid particle*

Let the time-dependent velocity component of a fluid particle in the Earth-fixed coordinate system be $\boldsymbol{U} = (u^X, u^Y, u^Z)$.

By applying the explicit expressions for the velocity components presented in § 3.2 in the moving coordinate system, the velocity components in the Earth-fixed coordinate system, when $Ut - X < 2\sqrt{2}|Y|$, are written as

$$\begin{bmatrix} u^X \\ u^Y \\ u^Z \end{bmatrix} = \mathrm{Re}\left\langle \begin{bmatrix} \mathcal{U}^x_o \\ \mathcal{U}^y_o \\ \mathcal{U}^z_o \end{bmatrix} \exp\left\{ \mathrm{i}\left[\kappa\sqrt{1+q_o^2}\,(Ut - X - q_o Y) + \pi/4 \right]\right\}\right\rangle. \tag{4.17}$$

As $Ut - X \geq 2\sqrt{2}|Y|$, the measured location is inside the Kelvin wedge and then the velocity components can be decomposed into components due to transverse and divergent waves

$$\begin{bmatrix} u^X \\ u^Y \\ u^Z \end{bmatrix} = \begin{bmatrix} u^X_+ \\ u^Y_+ \\ u^Z_+ \end{bmatrix} + \begin{bmatrix} u^X_- \\ u^Y_- \\ u^Z_- \end{bmatrix} \tag{4.18}$$

with

$$\begin{bmatrix} u^X_\pm \\ u^Y_\pm \\ u^Z_\pm \end{bmatrix} = \mathrm{Re}\left\langle \begin{bmatrix} \mathcal{U}^x_\pm \\ \mathcal{U}^y_\pm \\ \mathcal{U}^z_\pm \end{bmatrix} \exp\left\{ \mathrm{i}\left[\kappa\sqrt{1+q_\pm^2}\,(Ut - X - q_\pm Y) \mp \pi/4 \right]\right\}\right\rangle, \tag{4.19}$$

where vectors $[\mathcal{U}^x_o, \mathcal{U}^y_o, \mathcal{U}^z_o]^{\mathrm{T}}$ and $[\mathcal{U}^x_\pm, \mathcal{U}^y_\pm, \mathcal{U}^z_\pm]^{\mathrm{T}}$ are given by (3.11) and (3.7), respectively, and they are dependent on time t.

5. The inverse method

Based on the physical properties of the ship wake obtained in § 4, we present in this section an inverse method called the two-probe method for obtaining the moving speed and direction of the sailing ship. In contrast to the synthetic aperture radar image which can produce similar information (Reed & Milgram 2002; Zilman, Zapolski & Marom 2014; Karakuş *et al.* 2020), the method presented here is much simpler, because it builds upon the time record of the surface elevation at two fixed locations.

We assume that the surface elevation induced by waves generated by a ship moving at a constant speed has been recorded by two single-point probes located at points A and B, as depicted in figure 6. The distance between A and B is denoted by λ, and the angle between the ship's sailing line and the straight line crossing A and B is represented by θ, which is currently unknown and needs to be determined. Let t_A and t_B be the time instants when the cusp of the ship waves reaches probe A and B, respectively. By definition, we set

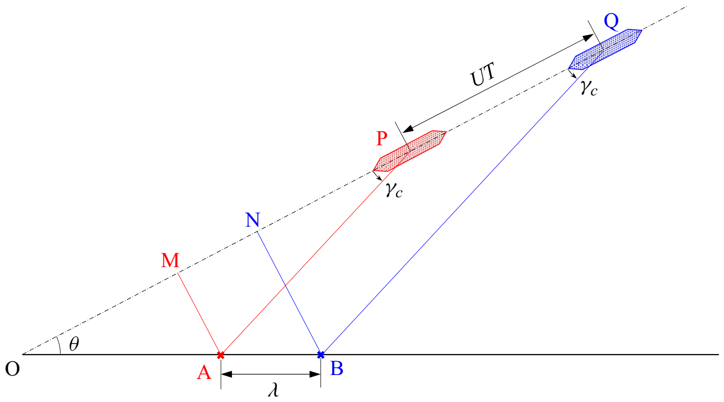

Figure 6. Diagram of the two-probe method for the ship's moving speed and direction. A and B are the locations of two fixed with a distance denoted by λ. The sailing direction with respect to the sensor deployment line is θ, which is to be determined. The cusp of the Kelvin wedge meets probes A and B when sailing at locations P and Q, respectively.

$T = t_B - t_A$. At time instants t_A and t_B, the centre of the ship is located at points P and Q, respectively, as indicated in figure 6.

By utilising the short-time Fourier transform, one can effectively separate components of different frequencies (Sheremet *et al.* 2013; Torsvik *et al.* 2015; Pethiyagoda *et al.* 2017; Liang *et al.* 2020*a*; Pethiyagoda *et al.* 2021; Buttle *et al.* 2022). This allows us to create an amplitude heat map representing the time and frequency variation of the waves. As a result, we can obtain the time-dependent wave frequencies $\omega_{\pm}^{A}$ and $\omega_{\pm}^{B}$ measured at locations A and B, respectively. Here, the subscripts $-$' and $+$' correspond to transverse and divergent waves, respectively. By obtaining the time difference T between the measurements at A and B, as defined earlier, we can proceed to determine the ship's speed denoted by U and its angle of motion relative to the straight line AB.

Based on the long-time asymptotic expression of transverse waves given by (4.13*a*,*b*), the ship's speed can be given by

$$U = g/\omega_{-}^{A,B} \quad \text{when transverse waves are in a steady state,} \tag{5.1}$$

due to the fact that the frequency of transverse waves is approximately independent of time according to figure 3.

To determine the sailing angle θ, we introduce the following geometric relation:

$$|\mathrm{MP}| + UT = |\mathrm{MN}| + |\mathrm{NQ}|. \tag{5.2}$$

The difference $|\mathrm{NQ}| - |\mathrm{MP}|$ can be replaced by

$$|\mathrm{NQ}| - |\mathrm{MP}| = 2\sqrt{2}(|\mathrm{BN}| - |\mathrm{AM}|), \quad \text{with } |\mathrm{BN}| - |\mathrm{AM}| = \lambda \sin\theta, \tag{5.3}$$

where the relation $\tan\gamma_c = 1/\sqrt{8}$ has been used. Then, the geometric relation (5.2) gives rise to the following relation:

$$UT = \lambda\cos\theta + 2\sqrt{2}\lambda\sin\theta, \tag{5.4}$$

which sets up a relation among λ, UT and θ. As a consequence, the angle between the deployment line and sailing line θ is obtained

$$\theta = \arcsin\left(\frac{UT}{3\lambda}\right) - \gamma_c, \tag{5.5}$$

which gives $\theta = 0$ for $UT = \lambda$, i.e. the ship track in parallel with the line $|AB|$.

Based on (4.13*a,b*), the frequency for divergent waves is linearly increasing with time at a slope defined as $S = g/(2Y_s)$. The measurement of the slope of the upper branch associated with divergent waves gives $S_A = g/(2Y_s^A)$ and $S_B = g/(2Y_s^B)$, and then the lateral distances from the sailing line Y_s^A and Y_s^B can be obtained. Suppose that the cusp line meets the probes A and B at time instants t_A and t_B, respectively. Then, we have

$$\frac{U(t_A - t_0)}{Y_s^A} = 2\sqrt{2} = \frac{U(t_B - t_0) - \lambda\cos\theta}{Y_s^B}, \tag{5.6}$$

where t_0 means the time instant when the midship is in alignment with probe A. Combining with (5.5), we obtain an equation with respect to θ

$$\theta = \arcsin\left[\frac{g}{2\lambda}\left(\frac{1}{S_B} - \frac{1}{S_A}\right)\right], \tag{5.7}$$

which determines the direction of the ship's course.

In summary, using the short-time Fourier transform in the two-point measurement method allows us to extract the relevant wave frequencies at locations A and B. This information, combined with the time difference T, enables us to determine the ship's velocity and its sailing direction with respect to the line AB. The two-point measurement method provides a simple but reliable and practical approach for estimating essential navigation parameters based on wave measurements at two distinct locations.

6. Results and discussions

For illustrative purposes, wave patterns generated by a parabolic Wigley hull model are considered, and the geometry of the Wigley hull is defined as

$$y = \pm\frac{L}{20}\left[1 - (2x/L)^2\right]\left[1 - (15z/L)^2\right], \tag{6.1}$$

which is applied in Buttle *et al.* (2022). In (6.1), L denotes the length of the Wigley hull, and the Froude number associated with the ship's speed is defined as $F = U/\sqrt{gL}$. It is noted that this model is applicable to ships of arbitrary geometry. This is made possible by utilising the Kochin function (2.9), which is directly linked to the wetted surface of the ship's hull. The application of the Hogner model for describing waves generated by a realistic ship hull can be found in Zhang *et al.* (2015) and Wu *et al.* (2019).

6.1. *Comparison with experiments and verification of the numerical model*

We compare the results obtained from the numerical computation of the wavenumber integral (2.8) with experimental measurements reported in Buttle *et al.* (2020). Figure 7 illustrates the time history of waves generated by a translating Wigley hull, as described in (6.1), at two distinct sensor locations. The lateral distances from the sailing line to the sensors are $Y_s = 2L$ (*a*) and $Y_s = 3L$ (*b*), respectively, and the Froude number is $F = 0.3259$. Despite the presence of noise in the experimental data, the agreement at both sensor locations is satisfactory, indicating the validity of the present numerical model. The good agreement between the numerical results and experimental measurements further indicates the reliability of the numerical model in capturing the wave patterns induced by a translating ship hull at sensor locations.

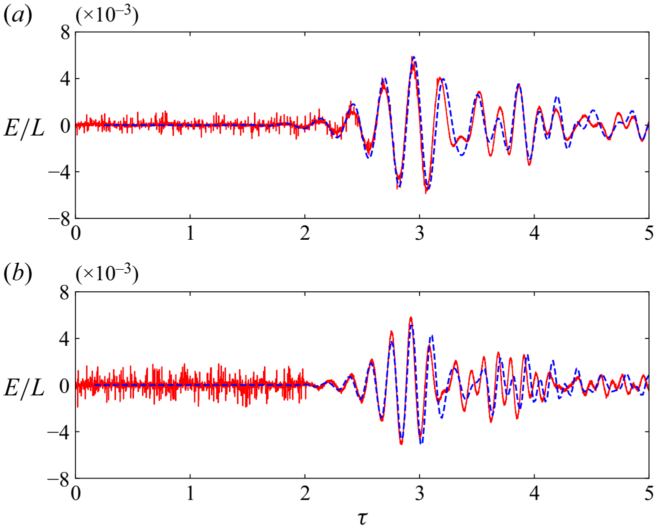

Figure 7. Time signal of the free surface elevation created by a Wigley hull at a forward speed $F = 0.3259$. Panels (*a*,*b*) correspond to the measurements at $Y_s = 2L$ and $Y_s = 3L$, respectively, from the sailing line. Comparison is made with the experiments reported in Buttle *et al.* (2020). Experiments: red solid line, numerical: blue dashed line.

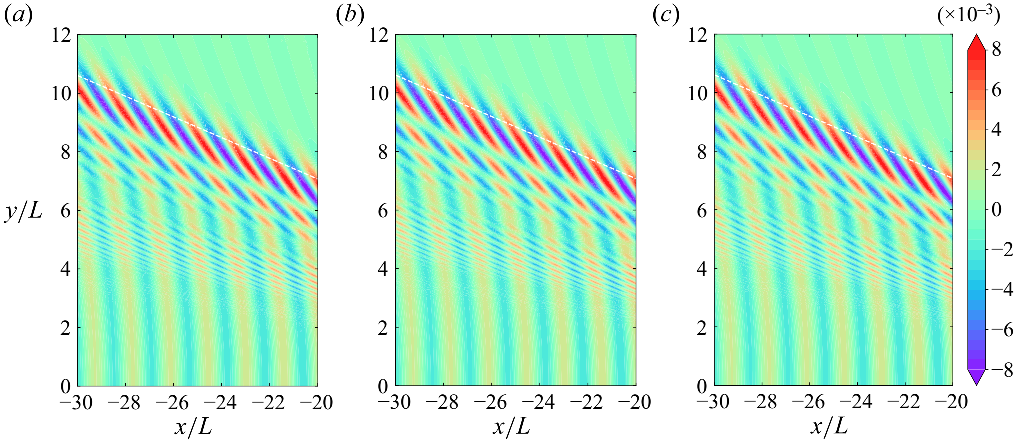

Figure 8. Wave patterns (E/L) generated by a translating Wigley hull at a Froude number $F = 0.5$ determined by direct numerical computation (*a*), CFU approximation (*b*) and KHP approximation (*c*).

To examine the accuracy of the KHP approximation elucidated in § 3, figure 8 exhibits the coloured plots of wave pattern created by a translating Wigley hull within the rectangular region $-30 \leq x/L \leq -20$, $0 \leq y/L \leq 12$ at a Froude number $F = 0.5$. The free surface elevation is normalised with respect to ship's length (E/L). Results determined by direct numerical integration, CFU approximation (Chester *et al.* 1957) and KHP approximation (Wu *et al.* 2018; Liang *et al.* 2020*b*) are displayed in panels (*a*,*b*,*c*), respectively. It is evident from the plots that there is no significant difference among the three panels, indicating that the KHP approximation accurately approximates the wavenumber integral (2.8).

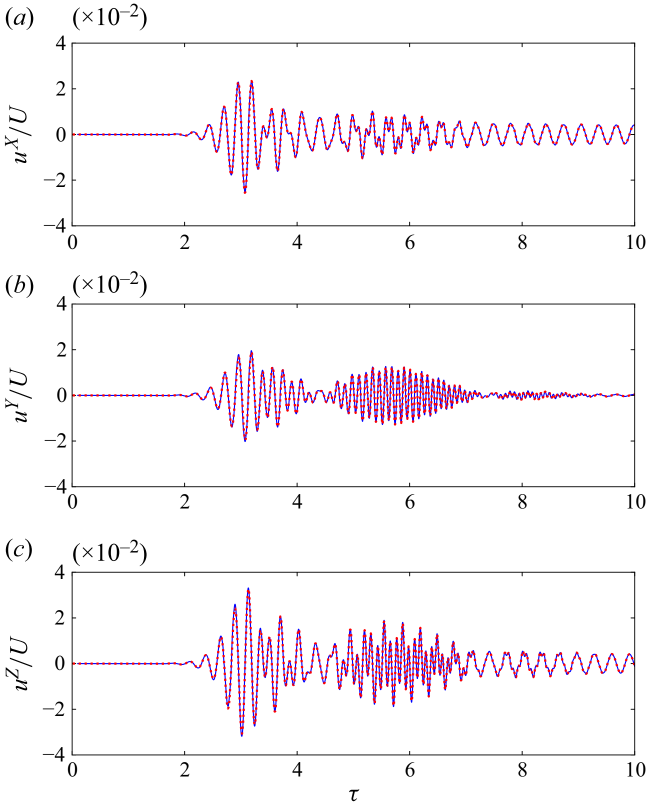

Figure 9. Non-dimensional induced velocity components $(u^X, u^Y, u^Z)/U$ measured at the Earth-fixed location $(X, Y, Z)/L = (0, 5, 0)$ varying with the non-dimensional time τ for $F = 0.5$. Comparison is made between the direction numerical integration (blue solid line) and the KHP approximation (red dotted line).

In figure 9, the induced velocity components $\boldsymbol{U} = (u^X, u^Y, u^Z)$ measured at an Earth-fixed location $(X, Y, Z)/L = (0, 5, 0)$ are presented as a function of non-dimensional time τ for the Froude number $F = 0.5$. The velocity components are non-dimensionalised with respect to the translating speed U. Comparison is made between the direction numerical integration of the wavenumber integral and the corresponding KHP approximation, and good agreement between the two methods is obtained.

The good agreement observed in figures 8 and 9 confirms the reliability of the KHP approximation for accurately predicting both the wave pattern and fluid particle velocities induced by a translating ship hull.

6.2. *Decomposition into transverse and divergent waves*

Figures 10, 11 and 12 exhibit coloured contour plots of wave patterns generated by the Wigley hull at Froude numbers $F = 0.2$, 0.5 and 0.7, respectively. The selected Froude numbers are associated with low-speed, medium-speed and high-speed vessels, respectively (Faltinsen 2005). The free surface elevation is normalised with respect to ship's length (E/L). Wave patterns, together with their decomposition into transverse and divergent waves inside the Kelvin wedge, are displayed in panels (*a,b,c*), respectively. The white dashed line in panel (*a*) corresponds to the cusp line of the Kelvin wake.

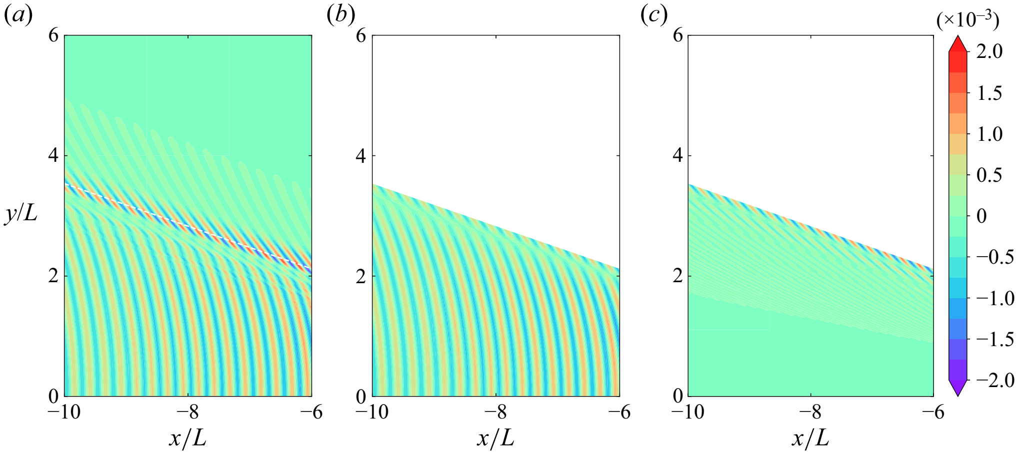

Figure 10. Wave patterns (a) as well as decomposition into transverse waves (b) and divergent waves (c) generated by a translating Wigley hull defined in (6.1) at a Froude number $F = 0.2$.

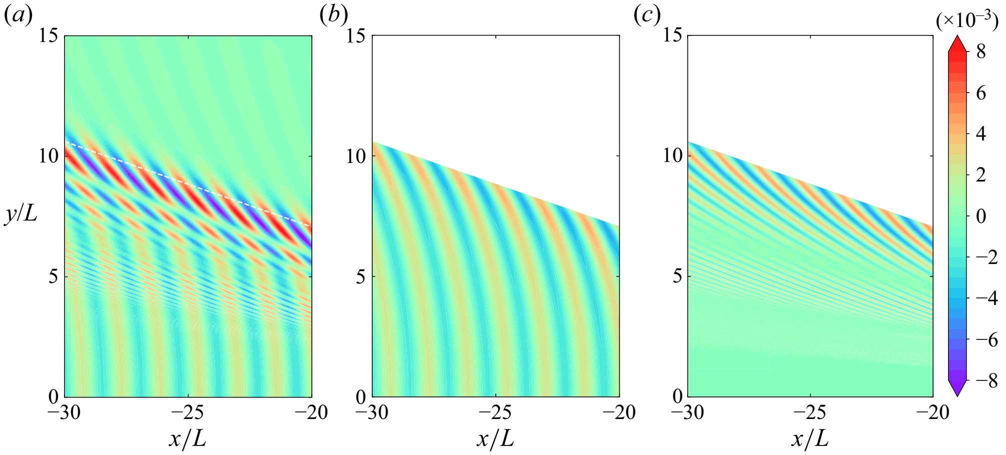

Figure 11. Same as figure 10, but $F = 0.5$.

At $F = 0.2$, the amplitude of transverse waves is appreciably larger than that of divergent waves, whereas the tendency is reversed at $F = 0.7$. The amplitudes of the two wave systems are comparable at $F = 0.5$. Therefore, divergent waves play an increasingly dominant role with increasing ship velocity, consistent with the conclusion that divergent waves are dominant for high-speed vessels (Faltinsen 2005; Darmon, Benzaquen & Raphaël 2014). In the panels (b,c), where transverse and divergent waves are displayed, respectively, the profiles are consistent with the iso-phase lines plotted in figure 1, and the wave crests are appreciably deflected near the cusp. In panel (a), wave patterns exhibit short-crested features as a consequence of superposition of transverse and divergent waves.

In figures 10–12, it is observed from the right panels that divergent waves vanish near the ship's track. This is because divergent waves near the track are associated with large wavenumbers, resulting in very short wavelengths according to the asymptotic analysis (Chen 2004; Liang & Chen 2018). Consequently, these short waves are significantly damped out under the influence of fluid viscosity effects (Liang & Chen 2019).

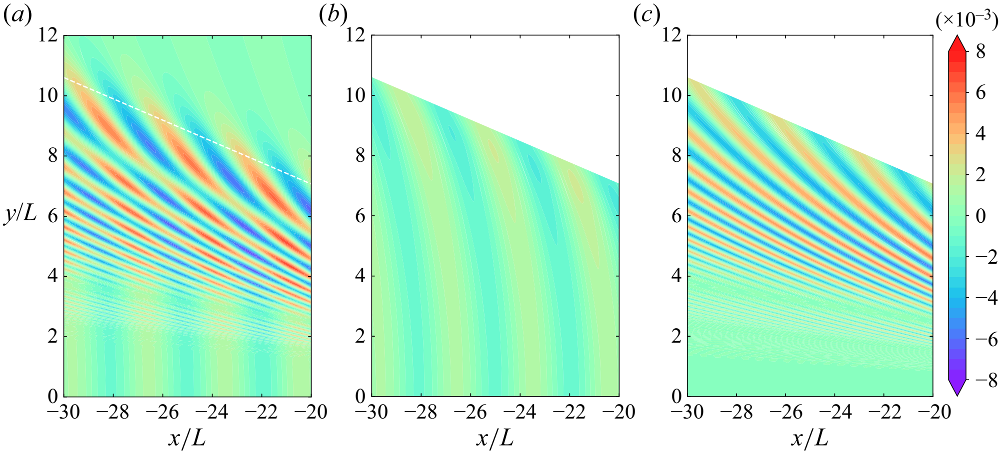

Figure 12. Same as figure 10, but $F = 0.7$.

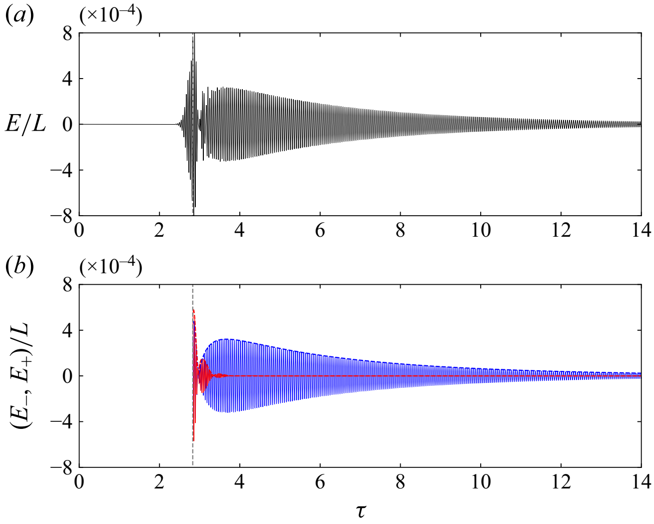

Figure 13. Time history of the ship wake E in panel (*a*) and the decomposition into transverse waves E_- (blue solid line) and divergent waves E_+ (red solid line) when $\tau \geq 2\sqrt{2}$ in panel (*b*). The corresponding amplitude functions $\|E_-\|$ and $\|E_+\|$ are plotted by dashed lines. The signal is measured at $(X, Y) = (0, 5L)$, and the Froude number is $F = 0.2$.

This observation explains the disappearance of divergent waves near the ship's track in the presented figures.

6.3. *Time responses at a fixed sensor location*

Figures 13, 14 and 15 depict the time histories of the ship wake measured at a fixed sensor location $(X, Y) = (0, 5L)$ for Froude numbers $F = 0.2$, 0.5 and 0.7, respectively. In panel (*a*) in each figure, the total signal E is displayed. When $\tau > 2\sqrt{2}$, the signal is further decomposed into transverse waves E_- and divergent waves E_+, which are shown in

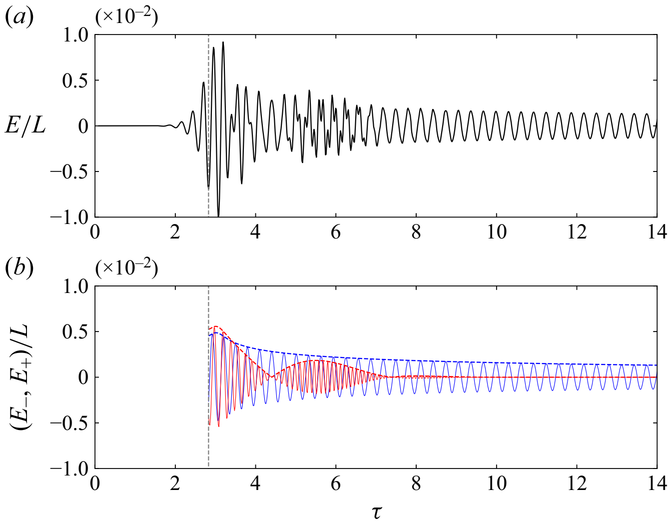

Figure 14. Same as figure 13, but $F = 0.5$.

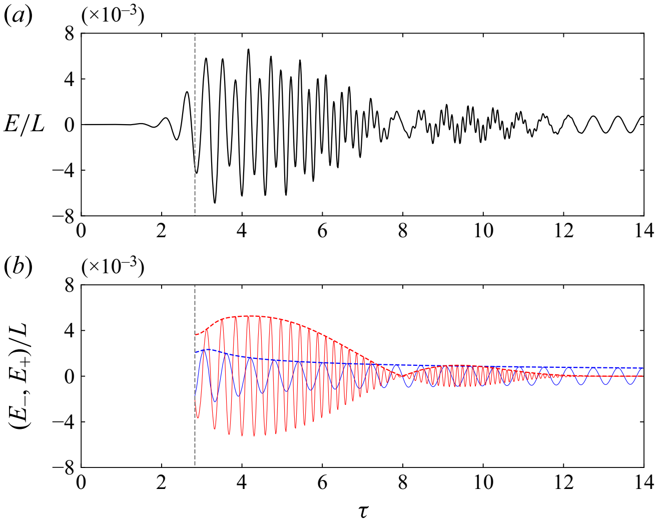

Figure 15. Same as figure 13, but $F = 0.7$.

panel (*b*) in each figure. Additionally, the corresponding amplitude functions (envelopes) $\|\mathcal{E}_-\|$ and $\|\mathcal{E}_+\|$, are plotted in panel (*b*) of each figure as dashed lines.

In the vicinity of the time instant $\tau = 2\sqrt{2}$, when the cusp line intersects the sensor, divergent waves play an increasingly significant role with higher ship speeds (larger Froude numbers). With time marching, the frequency of divergent waves increases steadily, as depicted in figure 3. However, despite this increase, divergent waves eventually decay to zero. At the sensor location, the lateral distance from the ship's sailing line remains constant, while the in-line distance consistently increases, resulting in a decreasing polar angle γ. As explained in Liang & Chen (2019), divergent waves experience considerable damping for small polar angles due to the influence of fluid viscosity effects. Consequently, the sensor can only measure divergent waves over a finite period of time. By comparing figures 13–15, we observe that the duration of divergent waves increases with the

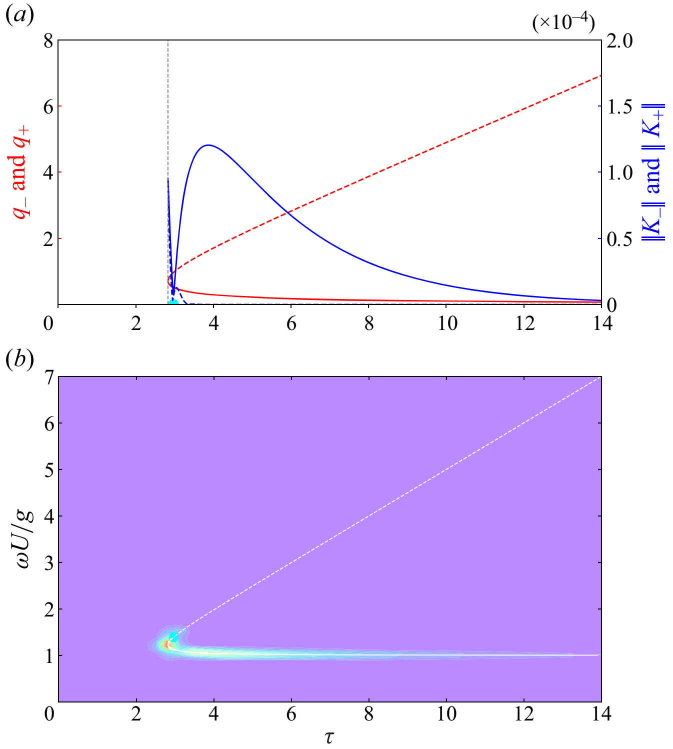

Figure 16. Stationary phase points $q_\pm$ defined by (3.1) and the corresponding Kochin functions $\|K_\pm\|$ in panel (*a*) and the time–frequency spectrogram obtained from the short-time Fourier transform in panel (*b*) at $F = 0.2$. The physical quantities associated with transverse waves are plotted by solid lines (——), and those with divergent waves are by dashed lines (- - - -). The cyan full circles (●, cyan) denote the locations where the amplitude of divergent waves is diminishing.

ship's speed. Consequently, the divergent waves generated by a high-speed ship may lead to highly transient responses of near-shore floating structures, which should be taken into account for engineering and safety considerations.

In contrast to divergent waves, the frequency of transverse waves remains nearly constant with time, and their wave amplitude decreases slowly, as depicted by the blue dashed line. Therefore, the influence of transverse waves at the sensor location will persist for an extended period. In panel (*b*) of the figures, it is observed that the envelope of divergent waves (red dashed line) undergoes modulation, leading to vanishing amplitude at certain locations. These locations correspond to the low-intensity regions in the divergent wave branch of time–frequency spectrograms, which are evident in both numerical simulations and experimental measurements (Pethiyagoda *et al.* 2018; Buttle *et al.* 2022). This modulation phenomenon contributes to the intermittent presence of divergent waves, causing variations in their amplitudes over time.

To explore the occurrence of vanishing amplitude in divergent waves at the probed location, we present two sets of plots. In panel (*a*), we show the time variation of the stationary phase points $q_\pm$ and the corresponding modulus of the Kochin functions $\|K_\pm\|$. Simultaneously, in panel (*b*), we present the time–frequency spectrograms obtained from the short-time Fourier transform using the `scipy` library in Python.

Figures 16, 17 and 18 correspond to Froude numbers $F = 0.2$, 0.5 and 0.7, respectively. When $\tau > 2\sqrt{2}$, the sensor is located within Kelvin's wedge, giving rise to the presence of

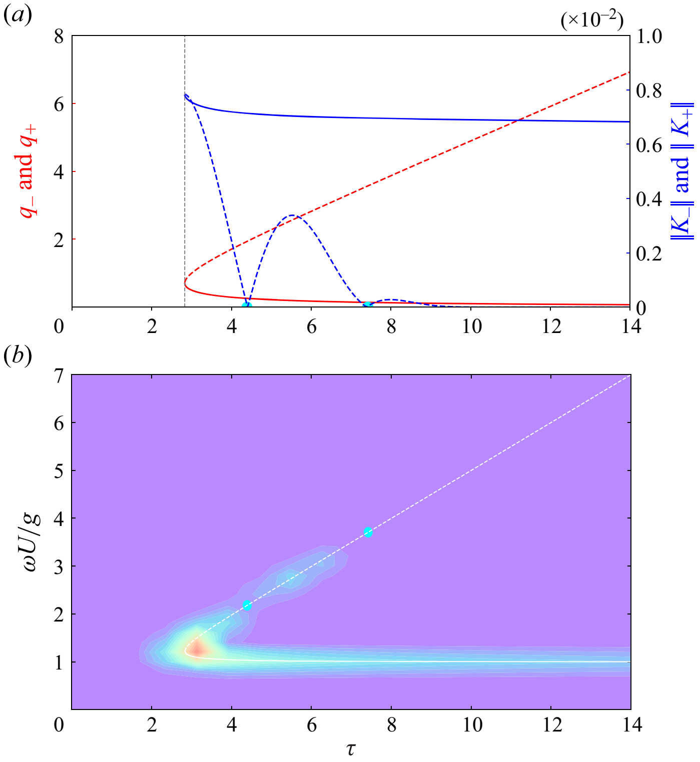

Figure 17. Same as figure 16, but $F = 0.5$.

two distinct stationary phase points, q_- and q_+, associated with transverse and divergent waves, respectively, as described in (3.1).

With the progression of time, the stationary phase point q_- gradually approaches zero, resulting in a mild variation of the Kochin function for transverse waves, $\|K_-\|$ with $K_\pm = K(q_\pm, -Ut)$ given by (2.9). In contrast, the stationary phase point q_+ continues to increase with time. As a consequence, the corresponding Kochin function $\|K_+\|$ undergoes modulation, leading to the occurrence of vanishing amplitude in divergent waves.

These locations, where the amplitude of divergent waves disappears, are denoted by cyan full circles, and they cause a discontinuity in the upper branch of the time–frequency spectrograms. This phenomenon provides insight into the intermittent presence of divergent waves and the patterns of amplitude variation in the vicinity of the sensor location.

6.4. *Velocity components of the fluid particle*

We now focus on examining the velocity components of fluid particles, measured at an Earth-fixed location $(X, Y, Z)/L = (0, 5, 0)$, induced by ship waves as a function of the non-dimensional time $\tau = Ut/Y$. These velocity components are normalised with respect to the ship's speed U. The results corresponding to Froude numbers $F = 0.2$, 0.5 and 0.7 are depicted in figures 19, 20 and 21, respectively. Within each figure, the velocity components u^X, u^Y and u^Z are respectively exhibited in panels (*a*), (*b*) and (*c*).

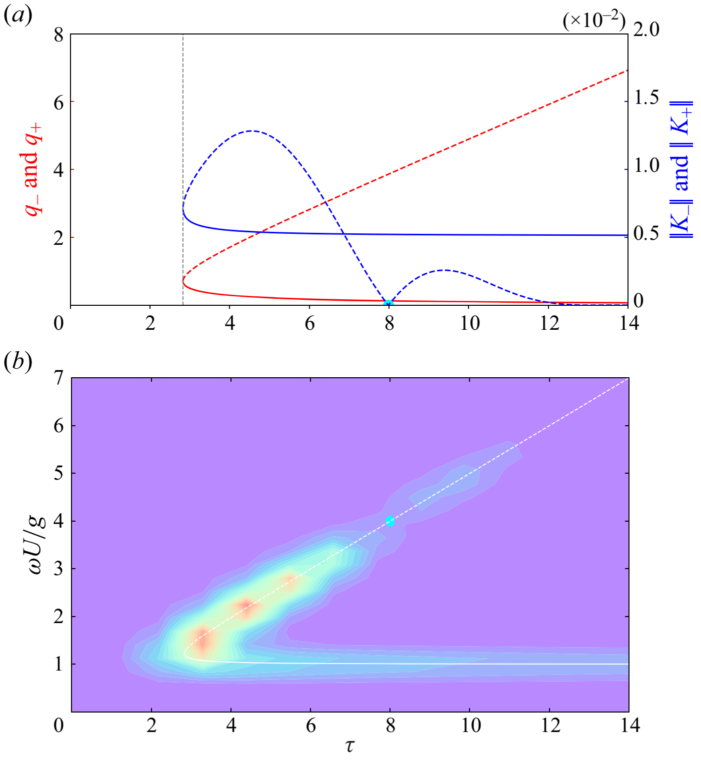

Figure 18. Same as figure 16, but $F = 0.7$.

The directional characteristics of transverse and divergent waves, as depicted in figure 4, reveal that transverse waves eventually propagate towards the ship's sailing direction, while divergent waves exhibit an increasing angle until they approach perpendicularity to the ship's course.

At a low Froude number $F = 0.2$, as in figure 19, the wave pattern predominantly comprises transverse waves that propagate in alignment with the ship's sailing path. Consequently, the velocity field is primarily influenced by components u^X and u^Z, while the lateral velocity component u^Y, mainly contributed by divergent waves, remains negligible. Upon reaching a Froude number of $F = 0.5$, as in figure 20, the significances of transverse and divergent waves become comparable, resulting in all three velocity components displaying comparable magnitudes. At a higher Froude number $F = 0.7$, as in figure 21), despite the existence of divergent waves within a finite period, their dominant influence is elucidated in § 6.2. Consequently, the velocity field is predominantly influenced by components u^Y and u^Z, while the in-line velocity component u^X, mainly attributed to transverse waves, becomes inconsequential.

6.5. *Showcase of the two-probe method*

To demonstrate the effectiveness of the two-point measurement method elucidated in § 5, we devise a problem with a ship model of length $L = 1$ m sailing at a speed $U = 1.6\ \mathrm{m\ s^{-1}}$. Two wave probes A and B are at a distance $\lambda = 2$ m, and the sailing direction with respect to the deployment line is $\theta = 30^\circ$.

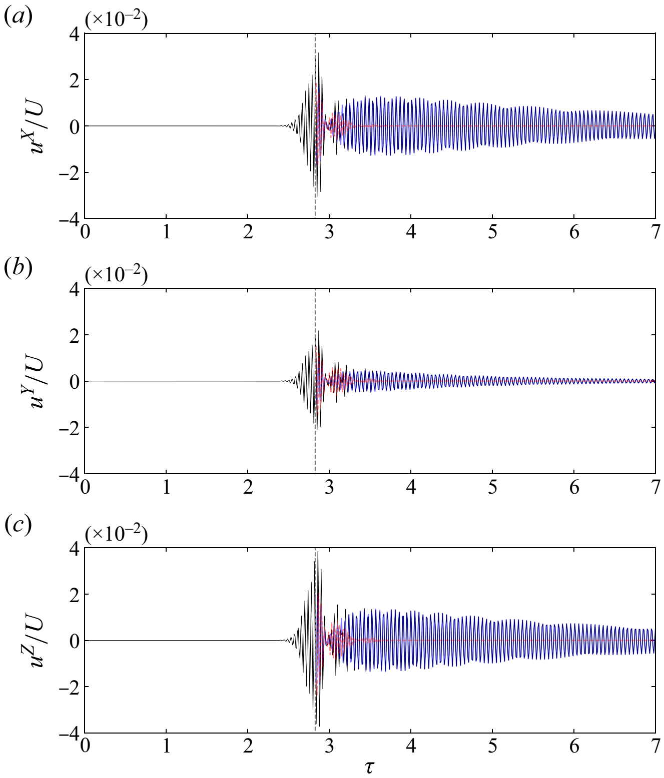

Figure 19. Time series of non-dimensional induced velocity components $(u^X, u^Y, u^Z)/U$ and their decomposition into the components due to transverse waves (blue solid line) and divergent waves (red dashed line). The velocity components are measured at an Earth-fixed location $(X, Y, Z)/L = (0, 5, 0)$ for the Froude number $F = 0.2$.

Figures 22 and 23 exhibit the time histories and the corresponding time–frequency spectrograms obtained from the measurements at probes A and B, respectively. By analysing the frequency of the lower branch of the spectrogram heat map, we determine the frequency of transverse waves as $\omega_- \approx 6.1\ \mathrm{rad\ s^{-1}}$. Consequently, using (5.1), we compute the corresponding velocity $U_{cal} \approx 1.61\ \mathrm{m\ s^{-1}}$, which is in close agreement with the true value of $1.6\ \mathrm{m\ s^{-1}}$.

By measuring the upper branch associated with divergent waves, we can obtain the slopes $S_A = g/(2Y_s^A) \approx 1.6$ and $S_B = g/(2Y_s^B) \approx 1.2$ of frequencies for divergent waves measured at probes A and B. Then, using the relation (5.7), we compute the sailing angle as $\theta_{cal} \approx 30.7^\circ$, which shows good agreement with the true value $\theta_{true} = 30^\circ$. The successful estimation of both the ship's speed and sailing angle through measurements of two branches in the heat map of the time–frequency spectrograms validates the effectiveness of the developed two-point method.

In conclusion, the two-probe method presented here provides a simple but reliable means to estimate the ship's speed and sailing angle by analysing two branches in the time–frequency spectrogram heat map. This method offers a practical solution for obtaining essential navigation information from wave measurements at two distinct locations, proving its potential for real-world applications.

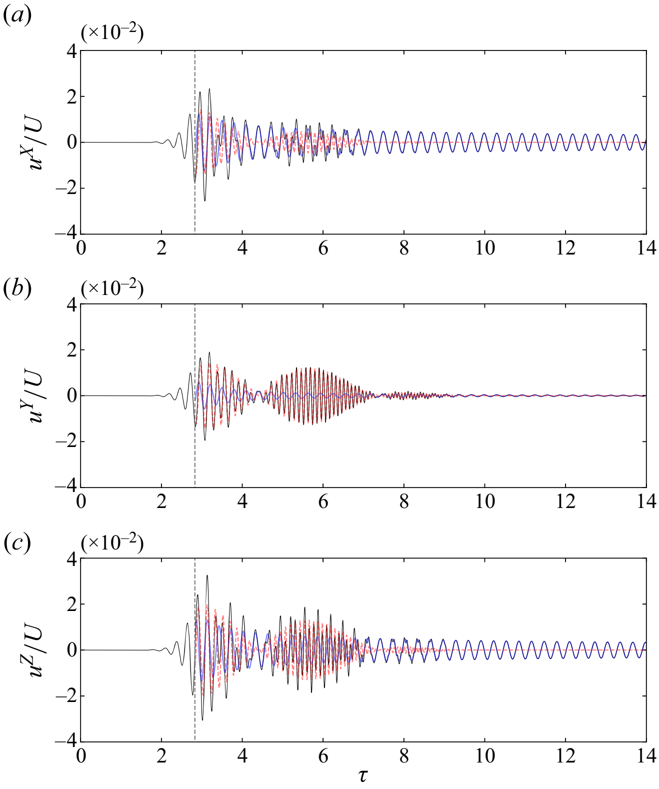

Figure 20. Same as figure 19, but $F = 0.5$.

7. Conclusions

This paper investigates the waves observed at fixed locations caused by the passage of a vessel moving at a constant speed. The study derives the physical properties of these waves, which have significant implications for coastal management and protection in the context of climate change and sea-level rise. By employing a combination of the Hogner model and the viscous-ship-wave Green function, we find that the waves are unsteady and exhibit short-crested features, despite the vessel's steady advancement.

The numerical model's validity has been confirmed through comparisons with experimental measurements, demonstrating good agreement. A uniform KHP approximation is used to represent the far-field waves generated by the ship and for the decomposition of the transverse and divergent waves. The physical properties of the transverse and divergent waves are explicitly obtained, including the amplitude, frequency, wavenumber, wave direction, phase velocity and group velocity.

We find that the physical properties of transverse and divergent waves measured at a fixed location can be summarised as follows.

(i) The frequency of transverse waves remains almost constant over time but is inversely proportional to the ship's speed. The frequency of divergent waves is independent of the ship's speed but increases linearly with time.

(ii) Both transverse and divergent waves exhibit that group velocities propagate in the same direction as the phase velocity. The magnitude of the group velocity is half that of the phase velocity, consistent with deep water wave theory.

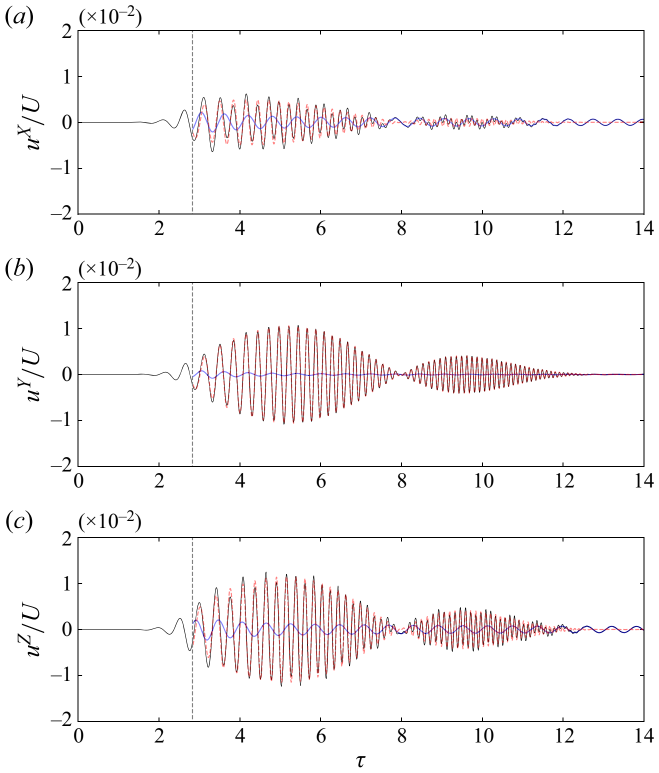

Figure 21. Same as figure 19, but $F = 0.7$.

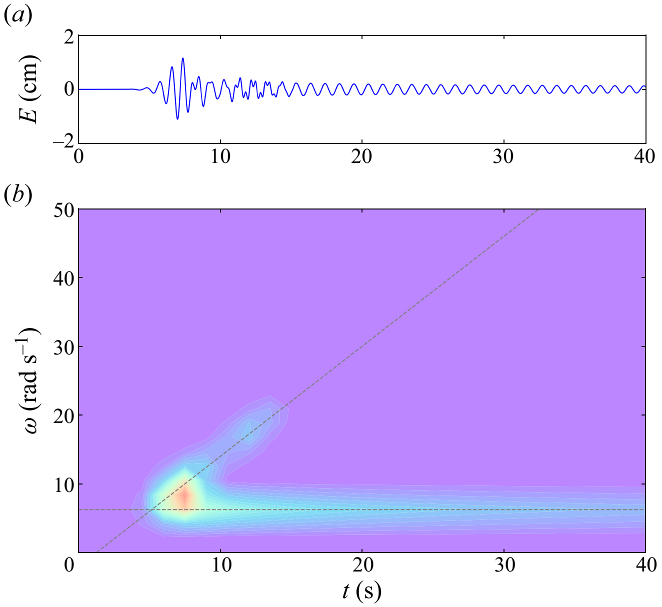

Figure 22. Free surface elevation measured at probe A (*a*), and the corresponding time–frequency spectrogram (*b*). Grey dashed lines in panel (*b*) correspond to asymptotic expressions (4.13*a*,*b*) for transverse and divergent waves.

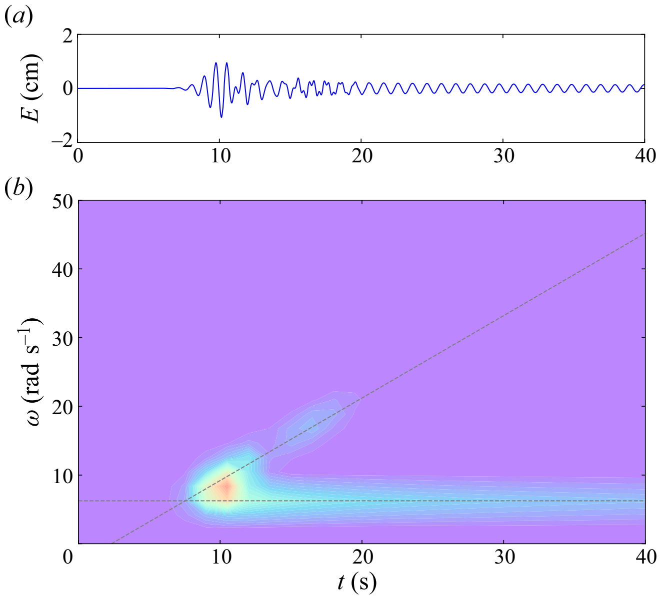

Figure 23. Same as figure 22, but at probe B.

- (iii) When the sensor encounters the cusp line of the Kelvin wake, the heading angles for transverse and divergent waves are identical, both measuring 35.26°. However, as time progresses, the wave propagation angle changes. Specifically, transverse waves will propagate in the direction of the ship's sailing, while divergent waves will propagate towards perpendicularity to the ship's sailing line. Therefore, the induced velocity component aligned with the ship's course is primarily influenced by transverse waves, while the lateral velocity component is dominated by divergent waves.
- (iv) A sensor fixed at a particular location can only measure divergent waves for a finite period, with the duration increasing as the ship's speed rises. On the other hand, transverse waves persist for an extended time and decay slowly with the passage of time.

The present study is focused on ship waves in deep water, which can be readily extended to more general cases, e.g. a finite water depth (Yang, Faltinsen & Zhao 2006; Zhu *et al.* 2015), ship waves in a background current (Ellingsen 2014; Li & Ellingsen 2016*b*), ship waves in the ambient ocean waves (Noblesse & Hendrix 1992; Chen 2004), etc. That being said, the main results obtained from this work are limited to linear and asymptotic waves sufficiently far away from the ship.

Acknowledgements. H.L. warmly thanks Dr R. Pethiyagoda for providing raw data of experiments.

Funding. This work is supported by A*STAR under its RIE 2020 Industry Alignment Fund, grant no. A19F1a0104 (ENSURE), and the National Research Foundation, Singapore and Singapore Maritime Institute under the Maritime Transformation Programme White Space Fund (Centre of Excellence for Autonomous and Remotely Operated Vessels (CEAOPS), Project ID SMI-2019-MTP-01). Y. Li acknowledges the support from the research council of Norway through the Fripro mobility grant (project no. 287389) and the POS-ERC project 342480.

Declaration of interests. The authors report no conflict of interest.

Author ORCIDs.
Hui Liang https://orcid.org/0000-0003-3602-1623;
Yan Li https://orcid.org/0000-0001-8925-3749;
Xiaobo Chen https://orcid.org/0000-0001-8288-2219.

Appendix A. Decomposition of the free surface term

In this appendix, the decomposition of the free surface term G^F into the local-flow and far-field wave components is considered. For convenience, physical variables are non-dimensionalised with respect to the translating speed U and gravitational acceleration g

$$(\tilde{x}, \tilde{y}, \tilde{z}) = \kappa(x-\xi, y-\eta, z+\zeta), \quad \mathcal{G}^F = G^F/\kappa, \tag{A1}$$

and then, the free surface term in the form of the double Fourier integral is expressed as (Liang & Chen 2019)

$$\mathcal{G}^F = \frac{2}{\pi}\mathrm{Re}\int_{-\infty}^{\infty}\int_0^{\infty}\frac{\exp(\tilde{z}\sqrt{\alpha^2+\beta^2}-\mathrm{i}(\alpha\tilde{x}+\beta\tilde{y}))}{\alpha^2-\sqrt{\alpha^2+\beta^2}-4\mathrm{i}\epsilon\alpha(\alpha^2+\beta^2)}\,\mathrm{d}\alpha\,\mathrm{d}\beta. \tag{A2}$$

The decomposition is realised by means of the Cauchy residue theorem. Equivalent but different from the analysis (Chen 2023) based on the polar coordinates (k, θ) with $(\alpha, \beta) = k(\cos\theta, \sin\theta)$ for the general case of the ship-motion Green function, here, we perform directly in (α, β) plan and take the α-integral as the inner integral. The root to the complex dispersion relation in the denominator of (A2) is (Lu & Chwang 2007)

$$\alpha(\beta) \approx a_0 + \mathrm{i}\epsilon a_1, \tag{A3a}$$

where

$$a_0 = \sqrt{\frac{1+m}{2}}, \quad \text{and} \quad a_1 = \frac{(1+m)^3}{2m}, \quad \text{with } m = \sqrt{1+4\beta^2}. \tag{A3b}$$

The wave component dominant in the far field is associated with the residue of the α-integral, and it is written in the form of a wavenumber integral (Liang & Chen 2019)

$$\mathcal{G}^W = -4H(-\tilde{x})\mathrm{Im}\int_{-\infty}^{\infty}\exp\left[(1+q^2)\tilde{z} + 4\epsilon\tilde{x}\frac{(1+q^2)^3}{1+2q^2} - \mathrm{i}\sqrt{1+q^2}(\tilde{x}+q\tilde{y})\right]\mathrm{d}q. \tag{A4}$$

Then, we are focused on the simplification of the local-flow component $\mathcal{G}^L$, which is missing in Liang & Chen (2019). Following Noblesse (1977), we simplify the integral with respect to α, and the corresponding α-integral is illustrated in figure 24. We may construct a closed contour including the integration path, a quarter circle with a radius $R \to \infty$ and a path along the imaginary axis. It can be verified that the integral along the quarter circle vanishes as the radius R tends to infinity. As for the selection of the path along the imaginary axis, it depends on the location of the flow field point upstream or downstream.

A.1. *The case $\tilde{x} < 0$*

When $\tilde{x} < 0$, i.e. downstream, the integration path is deformed to the imaginary axis integrating from 0 to i∞, as illustrated in figure 24(a), and the local-flow component in

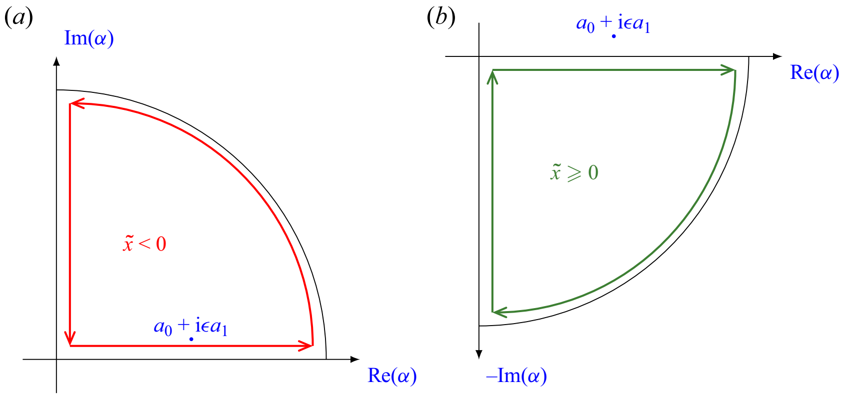

Figure 24. Integration contour in the complex $\alpha-$plane for $\tilde{x} < 0$ (*a*) and $\tilde{x} \geq 0$ (*b*).

this case is expressed as

$$\mathcal{G}^L = \frac{2}{\pi}\mathrm{Re}\int_{-\infty}^{\infty}\int_{0}^{\mathrm{i}\infty} \frac{\exp(\tilde{z}\sqrt{\alpha^2+\beta^2} - \mathrm{i}(\alpha\tilde{x}+\beta\tilde{y}))}{\alpha^2 - \sqrt{\alpha^2+\beta^2} - 4\mathrm{i}\epsilon\alpha(\alpha^2+\beta^2)}\,\mathrm{d}\alpha\,\mathrm{d}\beta. \tag{A5}$$

Introducing $\alpha = \mathrm{i}t$, (A5) is rewritten as

$$\mathcal{G}^L = \mathcal{G}_1^L + \mathcal{G}_2^L, \tag{A6a}$$

where $\mathcal{G}_1^L$ and $\mathcal{G}_2^L$ are written as

$$\mathcal{G}_1^L = \frac{2}{\pi}\mathrm{Re}\int_{-\infty}^{\infty}\int_{0}^{|\beta|} \frac{\mathrm{i}\exp(\tilde{z}\sqrt{\beta^2-t^2} - \mathrm{i}(\mathrm{i}t\tilde{x}+\beta\tilde{y}))}{-t^2 - \sqrt{\beta^2-t^2} + 4\epsilon t(\beta^2-t^2)}\,\mathrm{d}t\,\mathrm{d}\beta, \tag{A6b}$$

$$\mathcal{G}_2^L = \frac{2}{\pi}\mathrm{Re}\int_{-\infty}^{\infty}\int_{|\beta|}^{\infty} \frac{\mathrm{i}\exp(\mathrm{i}\tilde{z}\sqrt{t^2-\beta^2} - \mathrm{i}(\mathrm{i}t\tilde{x}+\beta\tilde{y}))}{-t^2 - \mathrm{i}\sqrt{t^2-\beta^2} + 4\epsilon t(t^2-\beta^2)}\,\mathrm{d}t\,\mathrm{d}\beta. \tag{A6c}$$

The integrand of $\mathcal{G}_1^L$ is an odd function with respect to β, and thus the component $\mathcal{G}_1^L$ is nil. By performing the variable of change $a = \sqrt{t^2-\beta^2}$, the representation of $\mathcal{G}^L$ is

$$\mathcal{G}^L = \frac{2}{\pi}\mathrm{Re}\int_{-\infty}^{\infty}\int_{0}^{\infty} \frac{\mathrm{i}a\exp(\mathrm{i}a\tilde{z} - \mathrm{i}(\mathrm{i}\tilde{x}\sqrt{a^2+\beta^2}+\tilde{y}\beta))}{[-(a^2+\beta^2) - \mathrm{i}a + 4\epsilon a^2\sqrt{a^2+\beta^2}]\sqrt{a^2+\beta^2}}\,\mathrm{d}a\,\mathrm{d}\beta. \tag{A7}$$

Converting the Cartesian coordinates (a, β) to polar coordinates via introducing $a = \varrho\cos\theta$ and $\beta = \varrho\sin\theta$, (A7) becomes

$$\mathcal{G}^L = \frac{2}{\pi}\mathrm{Re}\int_{-\pi/2}^{\pi/2}\int_{0}^{\infty} \frac{\mathrm{i}\cos\theta}{\sqrt{1+16\mathrm{i}\epsilon^2\cos^3\theta}}\left(\frac{1}{\varrho-\varrho_+} - \frac{1}{\varrho-\varrho_-}\right) \\ \times\exp(\varrho(\tilde{x}+\mathrm{i}\tilde{z}\cos\theta-\mathrm{i}\tilde{y}\sin\theta))\,\mathrm{d}\varrho\,\mathrm{d}\theta, \tag{A8a}$$

where ϱ_+ and ϱ_- are defined as

$$\varrho_+ = \frac{1+\sqrt{1+16\mathrm{i}\epsilon\cos^3\theta}}{8\epsilon\cos^2\theta} \approx \frac{1+4\mathrm{i}\epsilon\cos^3\theta}{4\epsilon\cos^2\theta}, \tag{A8b}$$

and

$$\varrho_- = \frac{1 - \sqrt{1 + 16\mathrm{i}\epsilon \cos^3\theta}}{8\epsilon \cos^2\theta} \approx -\mathrm{i}\cos\theta. \tag{A8c}$$

Using the relation in appendix C in Liang & Chen (2019), the double integral in (A2) reduces to a single integral

$$\mathcal{G}^L = \frac{2}{\pi}\mathrm{Re}\int_{-\pi/2}^{\pi/2} \frac{\mathrm{i}\cos\theta}{\sqrt{1 + 16\mathrm{i}\epsilon^2\cos^3\theta}}\left[\mathrm{e}^{Z_+}E_1(Z_+) - \mathrm{e}^{Z_-}E_1(Z_-)\right]\mathrm{d}\theta, \tag{A9a}$$

where $\mathrm{e}^u E_1(u)$ denotes the exponential-integral function, and $Z_\pm$ are defined as

$$Z_\pm = \varrho_\pm(\tilde{x} + \mathrm{i}\tilde{z}\cos\theta - \mathrm{i}\tilde{y}\sin\theta). \tag{A9b}$$

A.2. *The case $\tilde{x} \geq 0$*

Similar as the deformation of the contour integration performed in (A5), the integration path is deformed to the negative imaginary axis when $\tilde{x} \geq 0$, as illustrated in figure 24(*b*), and the corresponding local-flow component is

$$\mathcal{G}^L = \frac{2}{\pi}\mathrm{Re}\int_{-\infty}^{\infty}\int_{0}^{-\mathrm{i}\infty} \frac{\exp(\tilde{z}\sqrt{\alpha^2+\beta^2} - \mathrm{i}(\alpha\tilde{x} + \beta\tilde{y}))}{\alpha^2 - \sqrt{\alpha^2+\beta^2} - 4\mathrm{i}\epsilon\alpha(\alpha^2+\beta^2)}\,\mathrm{d}\alpha\,\mathrm{d}\beta. \tag{A10}$$

Introducing $\alpha = -\mathrm{i}t$, (A10) is rewritten as

$$\mathcal{G}^L = \mathcal{G}_1^L + \mathcal{G}_2^L, \tag{A11a}$$

where

$$\mathcal{G}_1^L = \frac{2}{\pi}\mathrm{Re}\int_{-\infty}^{\infty}\int_{0}^{|\beta|} \frac{-\mathrm{i}\exp(\tilde{z}\sqrt{\beta^2-t^2} - \mathrm{i}(-\mathrm{i}t\tilde{x} + \beta\tilde{y}))}{-t^2 - \sqrt{\beta^2-t^2} - 4\epsilon t(\beta^2-t^2)}\,\mathrm{d}t\,\mathrm{d}\beta, \tag{A11b}$$

$$\mathcal{G}_2^L = \frac{2}{\pi}\mathrm{Re}\int_{-\infty}^{\infty}\int_{|\beta|}^{\infty} \frac{-\mathrm{i}\exp(-\mathrm{i}\tilde{z}\sqrt{t^2-\beta^2} - \mathrm{i}(-\mathrm{i}t\tilde{x} + \beta\tilde{y}))}{-t^2 + \mathrm{i}\sqrt{t^2-\beta^2} + 4\epsilon t(t^2-\beta^2)}\,\mathrm{d}t\,\mathrm{d}\beta. \tag{A11c}$$

The same as (A6*b*), the integrand of $\mathcal{G}_1^L$ is an odd function with respect to β, and thus we have $\mathcal{G}_1^L = 0$. By performing successive change of variable as in (A7) and (A8*a*) and applying the relation in appendix C in Liang & Chen (2019), the local-flow component for $\tilde{x} \geq 0$ becomes

$$\mathcal{G}^L = -\frac{2}{\pi}\mathrm{Re}\int_{-\pi/2}^{\pi/2} \frac{\mathrm{i}\cos\theta}{\sqrt{1 - 16\mathrm{i}\epsilon^2\cos^3\theta}}\left[\mathrm{e}^{Z'_+}E_1(Z'_+) - \mathrm{e}^{Z'_-}E_1(Z'_-)\right]\mathrm{d}\theta, \tag{A12a}$$

where $Z'_\pm$ are defined as

$$Z'_\pm = \varrho'_\pm(-\tilde{x} - \mathrm{i}\tilde{z}\cos\theta - \mathrm{i}\tilde{y}\sin\theta), \tag{A12b}$$

with ϱ'_+ and ϱ'_- defined as

$$\varrho'_+ = \frac{1 + \sqrt{1 - 16\mathrm{i}\epsilon\cos^3\theta}}{8\epsilon\cos^2\theta} \approx \frac{1 - 4\mathrm{i}\epsilon\cos^3\theta}{4\epsilon\cos^2\theta}, \tag{A12c}$$

and

$$\varrho'_- = \frac{1 - \sqrt{1 - 16\mathrm{i}\epsilon\cos^3\theta}}{8\epsilon\cos^2\theta} \approx \mathrm{i}\cos\theta. \tag{A12d}$$

A.3. *Summary*

From (A9*b*) and (A12*b*), we note $Z^*_\pm = Z'_\pm$, where an asterisk means the complex conjugate. Recalling the following relation (Abramowitz & Stegun 1964):

$$[\mathrm{e}^{Z} E_1(Z)]^* = \mathrm{e}^{Z^*} E_1(Z^*), \tag{A13}$$

we can obtain a consistent local-flow component representation valid for both $\tilde{x} < 0$ and $\tilde{x} \geq 0$, and it is expressed as

$$\mathcal{G}^L = -\frac{2}{\pi}\mathrm{Im}\int_{-\pi/2}^{\pi/2} \cos\theta \left[\mathrm{e}^{Z_+}E_1(Z_+) - \mathrm{e}^{Z_-}E_1(Z_-)\right] \mathrm{d}\theta, \tag{A14a}$$

where $Z_\pm$ are defined as

$$Z_\pm = \varrho_\pm(-|\tilde{x}| + \mathrm{i}\tilde{z}\cos\theta - \mathrm{i}\tilde{y}\sin\theta). \tag{A14b}$$

Performing the change of variable $u = \sin\theta$, representation (A14*a*) becomes

$$\mathcal{G}^L = -\frac{2}{\pi}\mathrm{Im}\int_{-1}^{1} \left[\mathrm{e}^{\mathcal{Z}_+}E_1(\mathcal{Z}_+) - \mathrm{e}^{\mathcal{Z}_-}E_1(\mathcal{Z}_-)\right] \mathrm{d}u, \tag{A15a}$$

where $\mathcal{Z}_\pm$ are defined as

$$\mathcal{Z}_+ = \frac{1 + 4\mathrm{i}\epsilon(1-u^2)^{3/2}}{4\epsilon(1-u^2)}(-|\tilde{x}| + \mathrm{i}\tilde{z}\sqrt{1-u^2} - \mathrm{i}\tilde{y}u), \tag{A15b}$$

$$\mathcal{Z}_- = -\mathrm{i}\sqrt{1-u^2}(-|\tilde{x}| + \mathrm{i}\tilde{z}\sqrt{1-u^2} - \mathrm{i}\tilde{y}u). \tag{A15c}$$

Accounting for the asymptotic approximation for exponential-integral function of a large argument (Abramowitz & Stegun 1964)

$$\mathrm{e}^{u}E_1(u) = \frac{1}{u}\sum_{n=0}^{\infty}\frac{n!}{(-u)^n}, \tag{A16}$$

the local-flow component is approximated as

$$\mathcal{G}^L = \frac{2}{\pi}\mathrm{Im}\int_{-1}^{1} \mathrm{e}^{\mathcal{Z}}E_1(\mathcal{Z})\,\mathrm{d}u + O(\epsilon), \tag{A17a}$$

with

$$\mathcal{Z} = -\mathrm{i}\sqrt{1-u^2}(-|\tilde{x}| + \mathrm{i}\tilde{z}\sqrt{1-u^2} - \mathrm{i}\tilde{y}u). \tag{A17b}$$

REFERENCES

ABRAMOWITZ, M. & STEGUN, I.A. 1964 *Handbook of Mathematical Functions: with Formulas, Graphs, and Mathematical Tables*. National Bureau of Standards.

BECK, R.F., NEWMAN, J.N. & TUCK, E.O. 1975 Hydrodynamic forces on ships in dredged channels. *J. Ship Res.* **19** (3), 166–171.

BOURNE, J. 2000 Louisiana's vanishing wetlands: going, going... *Science* **289** (5486), 1860–1863.

BUTTLE, N.R., PETHIYAGODA, R., MORONEY, T.J., WINSHIP, B., MACFARLANE, G.J., BINNS, J.R. & MCCUE, S.W. 2020 Comparison of experimental and numerical ship wakes using time-frequency analysis. In *Proceeding of the 22nd Australasian Fluid Mechanics Conference, Brisbane, Australia, 7–10 December 2020* (ed. H. Chanson & R. Brown). AFMC.

BUTTLE, N.R., PETHIYAGODA, R., MORONEY, T.J., WINSHIP, B., MACFARLANE, G.J., BINNS, J.R. & MCCUE, S.W. 2022 Mathematical models and time-frequency heat maps for surface gravity waves generated by thin ships. Preprint arXiv:2205.01870.

CHEN, X.B. 2004 Analytical features of unsteady ship waves. In *Advances in Engineering Mechanics – Reflections and Outlook* (ed. A.T. Chwang, M.H. Teng & D.T. Valentine), pp. 371–389. World Scientific Publishing.

CHEN, X.B. 2023 Fundamental solutions to ship-motion problems with viscous effects. *Phys. Fluids* **35** (9), 097130.

CHEN, X.B. & WU, G.X. 2001 On singular and highly oscillatory properties of the Green function for ship motions. *J. Fluid Mech.* **445** (1), 77–91.

CHESTER, C., FRIEDMAN, B. & URSELL, F. 1957 An extension of the method of steepest descents. *Math. Proc. Camb. Phil. Soc.* **53** (3), 599–611.

CLARISSE, J.M. & NEWMAN, J.N. 1994 Evaluation of the wave-resistance Green function. III: the single integral near the singular axis. *J. Ship Res.* **38** (1), 1–8.

DARMON, A., BENZAQUEN, M. & RAPHAËL, E. 2014 Kelvin wake pattern at large Froude numbers. *J. Fluid Mech.* **738**, R3.

DIAS, F., DYACHENKO, A.I. & ZAKHAROV, V.E. 2008 Theory of weakly damped free-surface flows: a new formulation based on potential flow solutions. *Phys. Lett.* A **372** (8), 1297–1302.

DIDENKULOVA, I., SHEREMET, A., TORSVIK, T. & SOOMERE, T. 2013 Characteristic properties of different vessel wake signals. *J. Coast. Res.* **65**, 213–218.

ELLINGSEN, S.Å. 2014 Ship waves in the presence of uniform vorticity. *J. Fluid Mech.* **742**, R2.

FALTINSEN, O.M. 2005 *Hydrodynamics of High-Speed Marine Vehicles*. Cambridge University Press.

FONTAINE, E., FALTINSEN, O.M. & COINTE, R. 2000 New insight into the generation of ship bow waves. *J. Fluid Mech.* **421**, 15–38.

FORLINI, C., QAYYUM, R., MALEJ, M., LAM, M.-A.Y.-H., SHI, F., ANGELINI, C. & SHEREMET, A. 2021 On the problem of modeling the boat wake climate: the florida intracoastal waterway. *J. Geophys. Res.* **126** (2), e2020JC016676.

GABEL, F., LORENZ, S. & STOLL, S. 2017 Effects of ship-induced waves on aquatic ecosystems. *Sci. Total Environ.* **601**, 926–939.

HE, J., WU, H., YANG, C.-J., ZHU, R.-C., LI, W. & NOBLESSE, F. 2021 Boundary-integral representation sans waterline integral for flows around ships steadily advancing in calm water. *Eur. J. Mech. (B/Fluids)* **89**, 259–266.

HOGNER, E. 1923 Contributions to the theory of ship waves. *Ark. Mat. Astron. Fys.* **17** (12), 1–50.

KARAKUŞ, O., RIZAEV, I. & ACHIM, A. 2020 Ship wake detection in SAR images via sparse regularization. *IEEE Trans. Geosci. Remote Sens.* **58** (3), 1665–1677.

LI, Y. 2018 Wave-interference effects on far-field ship waves in the presence of a shear current. *J. Ship Res.*, **62** (1), 37–47.

LI, Y. & ELLINGSEN, S.Å. 2015 Initial value problems for water waves in the presence of a shear current. In *Proceedings of the 25th International Offshore and Polar Engineering Conference (ISOPE-2015) Kona, Hawaii* (ed. J.S. Chung, F. Vorpahl, S.Y. Hong, T. Kokkinis & A.M. Wang). ISOPE.

LI, Y. & ELLINGSEN, S.Å. 2016*a* Multiple resonances of a moving, oscillating surface disturbance on a shear current. *J. Fluid Mech.* **808**, 668–689.

LI, Y. & ELLINGSEN, S.Å. 2016*b* Ship waves on uniform shear current at finite depth: wave resistance and critical velocity. *J. Fluid Mech.* **791**, 539–567.

LI, Y., SMELTZER, B.K. & ELLINGSEN, S. 2019 Transient wave resistance upon a real shear current. *Eur. J. Mech. (B/Fluids)* **73**, 180–192.

LIANG, H. & CHEN, X.B. 2018 Asymptotic analysis of capillary-gravity waves generated by a moving disturbance. *Eur. J. Mech. (B/Fluids)* **72**, 624–630.

LIANG, H. & CHEN, X.B. 2019 Viscous effects on the fundamental solution to ship waves. *J. Fluid Mech.* **879**, 744–774.

LIANG, H., LI, Y. & CHEN, X. 2023 Physical properties of the ship wake and its detection. In *Proceeding of the 38th International Workshop on Water Waves and Floating Bodies, Michigan, USA* (ed. R. Beck & K. Maki).

LIANG, H., SANTO, H., SHAO, Y., LAW, Y.Z. & CHAN, E.S. 2020*a* Liquid sloshing in an upright circular tank under periodic and transient excitations. *Phys. Rev. Fluids* **5** (8), 084801.

LIANG, H., SANTO, H. & SI, M. 2022 Decomposition of ship waves and time-frequency spectrograms. In *Proceeding of the 37th International Workshop on Water Waves and Floating Bodies, Giardini Naxos, Italy* (ed. A. Iafrati & G. Colicchio).

Liang, H., Wu, H., He, J. & Noblesse, F. 2020*b* Kelvin–Havelock–Peters approximations to a classical generic wave integral. *Appl. Math. Model.* **77**, 950–962.

Lighthill, M.J. 1978 *Waves in Fluids*. Cambridge University Press.

Liu, A.K., Peng, C.Y. & Chang, S.Y.-S. 1997 Wavelet analysis of satellite images for coastal watch. *IEEE J. Ocean. Engng* **22** (1), 9–17.

Lu, D.-Q. & Chwang, A.T. 2007 Interfacial viscous ship waves near the cusp lines. *Wave Motion* **44** (7–8), 563–572.

Lyden, J.D., Hammond, R.R., Lyzenga, D.R. & Shuchman, R.A. 1988 Synthetic aperture radar imaging of surface ship wakes. *J. Geophys. Res.* **93** (C10), 12293–12303.

Meyers, S.D., Luther, M.E., Ringuet, S., Raulerson, G., Sherwood, E., Conrad, K. & Basili, G. 2021 Ship wakes and their potential shoreline impact in Tampa Bay. *Ocean Coast. Manage.* **211**, 105749.

Nakos, D.E. & Sclavounos, P.D. 1990 On steady and unsteady ship wave patterns. *J. Fluid Mech.* **215**, 263–288.

Newman, J.N. 1977 *Marine Hydrodynamics*. Massachusetts Institute of Technology Press.

Noblesse, F. 1977 The fundamental solution in the theory of steady motion of a ship. *J. Ship Res.* **21** (2), 82–88.

Noblesse, F., He, J., Zhu, Y., Hong, L., Zhang, C., Zhu, R. & Yang, C. 2014 Why can ship wakes appear narrower than Kelvin's angle? *Eur. J. Mech. (B/Fluids)* **46**, 164–171.

Noblesse, F. & Hendrix, D. 1992 On the theory of potential flow about a ship advancing in waves. *J. Ship Res.* **36** (1), 17–29.

Noblesse, F., Huang, F. & Yang, C. 2013 The Neumann–Michell theory of ship waves. *J. Engng Maths* **79** (1), 51–71.

Pethiyagoda, R., McCue, S.W. & Moroney, T.J. 2017 Spectrograms of ship wakes: identifying linear and nonlinear wave signals. *J. Fluid Mech.* **811**, 189–209.

Pethiyagoda, R., Moroney, T.J., Macfarlane, G.J., Binns, J.R. & McCue, S.W. 2018 Time-frequency analysis of ship wave patterns in shallow water: modelling and experiments. *Ocean Engng* **158**, 123–131.

Pethiyagoda, R., Moroney, T.J., Macfarlane, G.J. & McCue, S.W. 2021 Spectrogram analysis of surface elevation signals due to accelerating ships. *Phys. Rev. Fluids* **6** (10), 104803.

Rabaud, M. & Moisy, F. 2013 Ship wakes: Kelvin or Mach angle? *Phys. Rev. Lett.* **110** (21), 214503.

Rapaglia, J., Zaggia, L., Parnell, K., Lorenzetti, G. & Vafeidis, A.T. 2015 Ship-wake induced sediment remobilization: effects and proposed management strategies for the Venice Lagoon. *Ocean Coast. Manage.* **110**, 1–11.

Reed, A.M. & Milgram, J.H. 2002 Ship wakes and their radar images. *Annu. Rev. Fluid Mech.* **34** (1), 469–502.

Scarpa, G.M., Zaggia, L., Manfè, G., Lorenzetti, G., Parnell, K., Soomere, T., Rapaglia, J. & Molinaroli, E. 2019 The effects of ship wakes in the Venice Lagoon and implications for the sustainability of shipping in coastal waters. *Sci. Rep.* **9** (1), 1–14.

Sheremet, A., Gravois, U. & Tian, M. 2013 Boat-wake statistics at Jensen Beach, Florida. *ASCE J. Waterway Port Coastal Ocean Engng* **139**, 286–294.

Soomere, T. 2007 Nonlinear components of ship wake waves. *Appl. Mech. Rev.* **60**, 120–138.

Thomson, W. 1887 On the waves produced by a single impulse in water of any depth, or in a dispersive medium. *Proc. R. Soc. Lond.* A **42** (251–257), 80–83.

Torsvik, T., Soomere, T., Didenkulova, I. & Sheremet, A. 2015 Identification of ship wake structures by a time–frequency method. *J. Fluid Mech.* **765**, 229–251.

Ursell, F. 1960 On Kelvin's ship-wave pattern. *J. Fluid Mech.* **8** (3), 418–431.

Wehausen, J.V. 1973 The wave resistance of ships. *Adv. Appl. Mech.* **13**, 93–245.

Wu, H., He, J., Liang, H. & Noblesse, F. 2019 Influence of Froude number and submergence depth on wave patterns. *Eur. J. Mech. (B/Fluids)* **75**, 258–270.

Wu, H., He, J., Zhu, Y. & Noblesse, F. 2018 The Kelvin–Havelock–Peters farfield approximation to ship waves. *Eur. J. Mech. (B/Fluids)* **70**, 93–101.

Wyatt, D.C. & Hall, R.E. 1988 Analysis of ship-generated surface waves using a method based upon the local Fourier transform. *J. Geophys. Res.* **93** (C11), 14133–14164.

Yang, Q., Faltinsen, O.M. & Zhao, R. 2006 Green function of steady motion in finite water. *J. Ship Res.* **50** (2), 120–137.

Yeung, R.W. 1972 Sinkage and trim in first-order thin-ship theory. *J. Ship Res.* **16** (1), 47–59.

Yuan, Z.-M., Chen, M., Jia, L., Ji, C. & Incecik, A. 2021 Wave-riding and wave-passing by ducklings in formation swimming. *J. Fluid Mech.* **928**, R2.

ZHANG, C., HE, J., ZHU, Y., YANG, C.-J., LI, W., ZHU, Y., LIN, M. & NOBLESSE, F. 2015 Interference effects on the Kelvin wake of a monohull ship represented via a continuous distribution of sources. *Eur. J. Mech. (B/Fluids)* **51**, 27–36.

ZHU, Y., HE, J., ZHANG, C., WU, H., WAN, D., ZHU, R. & NOBLESSE, F. 2015 Farfield waves created by a monohull ship in shallow water. *Eur. J. Mech. (B/Fluids)* **49**, 226–234.

ZILMAN, G., ZAPOLSKI, A. & MAROM, M. 2014 On detectability of a ship's Kelvin wake in simulated SAR images of rough sea surface. *IEEE Trans. Geosci. Remote Sens.* **53** (2), 609–619.